Sequential Estimator for Breathing and Heart Beat Frequencies Using Radar

Guigeng Su

TU Delft

Sequential Estimator for Breathing and Heart Beat Frequencies Using Radar

by

Guigeng Su

to obtain the degree of Master of Science
at Delft University of Technology,
to be defended publicly on Wednesday August 28, 2019 at 13:30 PM.

Student number:	4710800	
Project duration:	January 1, 2019 – August 20, 2019	
Thesis committee:	Prof. dr. Alexander Yarovoy,	TU Delft, supervisor
	Dr. ir. Bert Jan Kooij,	TU Delft
	Prof. dr. Paddy French,	TU Delft
	Dr. Nikita Petrov,	TU Delft, supervisor

TU Delft

Contents

1 Introduction

1.1. Motivation

In the past decade, a great deal of attention has been drawn to the vital signs detection in various fields of modern life with the ever-increasing needs of security or health care [1, 2]. Respiratory rate and heart beat rate are two most important components of vital signs which are the main features while detecting or monitoring the health conditions of human beings. Traditional methods of vital signs monitoring, including electrocardiography (ECG) analysis with straps and electrodes are applicable with intrusive or contact devices and photoplethysmography (PPG), which has essential limitations in multiple scenarios such as burned skin, sudden infant death syndrome (SIDS), etc. [3–5]. Besides, with rapid development of smart houses or automotives, the desire of contactless vital signs monitoring is dramatically growing while radar technology is considered as one of the most promising methods.

Contactless vital signs detection or monitoring is mainly based on the periodic motion of the chest due to the cardiopulmonary activity. The study of radar technology for vital signs detection can be traced back to the 1970's which utilizes the radar's ability to detect the motion of respiratory movement [6]. Later, more research was conducted to improve the accuracy and reliability of vital signs detection, *e.g.* [7–9].

1.2. Existing approaches and goals of the thesis

Two types of radars are commonly used for vital signs monitoring: ultra wideband (UWB) radar and continuous wave (CW) radar.

According to the definition provided by Federal Communications Commission (FCC) and modified in 2002, a device is called UWB when its operational fractional bandwidth

$B/f_c > 0.20$ or when its absolute bandwidth $B > 0.5$ GHz [10]. Short pulses were used in first UWB radars and in some modern ones. The larger the bandwidth of the pulses is, the shorter is the duration time of the pulses, minimizing multipath interference [11]. However, they suffer from the complexity of its range profile resulting from different reflection properties at different layers of the human body and the widening effect on frequency spectrum at high frequencies of the signal [12]. Most of modern UWB radars transmits chirps with large duty cycle and obtain high range resolution by range compression. Besides, the monitoring of heart beat rate requires downrange accuracy of 0.3 mm [13], thus much higher bandwidth is needed, resulting in higher cost of the radar system.

Unmodulated continuous wave (CW) radar, referred to as Doppler radar, provides good performance in measuring target motion parameters by simply evaluating the phase change at each moment. Therefore, using the phase of one radio frequency, minor displacement of skin on the chest of the human body caused by breathing and heart beat can be detected [14]. This is achieved by applying interferometric theory, *i.e.*, only relative movement is measured. One major disadvantage of this technique is that Doppler radar is not able to determine the ranges of possible targets and further, not able to know which target is measured if there is more than one target observed since its signal is continuously transmitted and one cannot distinguish those reflected signals from different targets within the area of measurement in the received signal.

In order to overcome these drawbacks mentioned above, frequency modulation continuous wave (FMCW) radar technique is considered by taking its advantage of being able to estimate ranges of different targets while monitoring their vital signs. By taking the beat frequency between the transmitted signal and received signals, range estimation can be done. And by taking the phase evaluation of specific beat frequency in its range profile, the accuracy of minor displacement measurement can be achieved up to a few micrometers [15], much less than the typical displacements induced by respiration (ranging from 3 mm to 11 mm [16]), and the ones caused by heartbeat (ranging from 0.3 mm to 0.8 mm [13]) so vitals signs are detectable with this technique.

In the application scenario in automotives, a multiple-input and multiple-output (MIMO) system is considered in order to focus our estimator in a certain direction. With antenna array, direction of arrival (DoA) can be estimated, *i.e.*, azimuthal information can be obtained. Together with beamforming technique for MIMO system, clutter in the other direction can be eliminated thus increasing SCR of the signal in desired direction. Additionally, azimuth positioning can be achieved with MIMO system to help radar localize the position of the target in 2D plane horizontally or even in 3D space. With one dimension array, the spatial room inside auto are divided into a 2D matrix whose pixels

are defined by the cross- and down-range resolutions of the radar system. Vital signs detection and monitoring algorithms are then implemented in each pixel. Therefore, different passengers in automotive can be separated and monitored simultaneously.

Extensive research has been done in different aspects to measure the vital signs. They often have to deal with low signal-to-noise ratio (SNR) and low signal-to-clutter ratio (SCR) of the reflected signal and multiple targets can be present in the observed area. The MIMO system is used in multi-person scenarios and is able to estimate their DoAs while focusing the signals in desired directions and reducing clutter from other directions at the meantime, as presented in [17]. J. Aho *et al.* [18] demonstrated that vital signs measurement can be performed with a multi-antenna system and various adaptive signal processing techniques to increase SNR and improve measurement accuracy. S. Wang *et al.* [19] monitored vital signs using the UWB 80GHz FMCW radar and showed the possibility to detect respiration rate from the left side of the human body with a relatively low error rate. S. Ayhan *et al.* [20] demonstrated their measurements of vital signs with a 96GHz radar with both time and frequency method. Doppler phase history is extracted for estimating frequencies of both breathing and heart rate [21]. The statistical algorithm with wavelet decomposition is used to analyze heart beat in term of the phase history in [22]. Independent component analysis of respiration and heart rate with a Doppler radar designed to operate with a Phase-Locked-Loop (PLL) in phase demodulation stage is performed to retrieve respiratory and heart rate information from baseband signal in [23]. Random body movement can be cancelled by taking data from both sides of human body and performing complex signal demodulation [24]. Arctangent demodulation is proposed to solve the problem of DC offsets occurring at both in-phase and quadrature channels in [25]. Undesired clutter can be suppressed by applying the principle component analysis (PCA) as shown in [26]. However, these studies are mainly focusing on monitoring the vital signs either in simply scenario, or with a long-term observation time (*e.g.* 10 s or above) rather than sequential tracking. However, sequential tracking of vital signs has not been investigated yes. At the same time, in the closely related field of tracking human activities, Kalman filter and particle filter are widely applied *e.g.* [27–29].

Although many works has been done for vital signs detection, a great deal of challenges still exist. Separate measurements of vital signs in case of multiple persons and multi-path environment is necessary considering complicated real scenarios. The amplitudes of both two vital signs, respiration and heartbeat, are very weak to be detected since their non-contact detection is based on the minor movement on the surface skin on the chest, as explained in Chapter 2. The power of the signals from the chest is much lower compared to the power of clutter, resulting in low SCR. Moreover, perfect models

of vital signs does not exist, which poses additional uncertainty to their monitoring. Together with the problems of too many unknown parameters of vital signs and extra phase due to range, vital signs tracking is challenging.

In this thesis, a sequential estimator is proposed to track the features of vital signs, including the frequency and amplitude of both respiration and heartbeat. The estimator is used with a 77GHz commercial mm-wave radar. Simulations based on microwave propagation model and radar signal models have been done to evaluate the performance of the proposed estimator together with the real experimental verification.

1.3. Outline of the Thesis

The thesis is structured as follows. Chapter 2 introduces and describes the physiology of the cardiopulmonary activity, breathing and heart beats. In addition, the signal model for linear frequency modulation continuous wave (LFMCW) radar technology is presented in detail. In Chapter 3, accurate motion tracking of cardiopulmonary activity is demonstrated by extracting phase history and estimators for frequencies and amplitudes of vital signs are introduced. These methods are evaluated in numerical simulations and improved with some modifications in Chapter 4. Experimental verification is then presented in Chapter 5. Finally, both results and their corresponding contributions are summarized in Chapter 6.

2

Models for Vital Sign Monitoring

With the radar's ability to detect vital signs, non contact monitoring become possible, which does not constrain human activity and be preformed continuously. This great advantage of non contact monitoring is that it can be used to detect and record householders' vital signs activities in future smart house or the drivers' and customers' conditions in future automobiles.

In this chapter, the technology of linear frequency modulation continuous wave (LFMCW) radar is first demonstrated, together with its signal model. By analyzing the structure of the signal, the radar demonstrates itself the ability to reduce the signal-to-clutter (SCR) ratio by range cell isolation and shows the relationship between vital signs activity and phase shift in the particular range cell. The basic physiology behind cardiopulmonary is then introduced with its simplified mathematical models. The radar responses of vital signs are presented and analyzed with different mathematical models introduced previously.

2.1. LFMCW Radar

Since range resolution of radar is usually determined by the limited operational bandwidth, accurate movement of vital signs cannot be tracked. For example, a modern commercial radar operating at center frequency of $f_c = 77$ GHz with a bandwidth of $B = 4$ GHz provides range resolution of $\delta_r = 37.5$ mm, larger than $\Delta R = 11$ mm, the maximum possible displacement of vital signs. Therefore, the relative motion of the chest should be measured which is exactly the aim of vital signs detection. In order to endue radar with the ability to monitor multiple targets simultaneously, LFMCW technology is used. This ability also contributes to the reduction of SCR by separating

targets into different range cells.

In this section, the basic theory of LFMCW radar is described. And by analyzing its signal processing and their derivations, demonstrate its ability to determine the range and velocity of obsrved targets.

2.1.1. LFMCW Signal Model

LFM, as the term suggests, is featured by it instantaneous changing frequency within each pulse called sweep or chirp, and can be expressed as:

$$f(t) = f_c + \frac{B}{T_c}t = f_c + \beta t, \quad t \in [0, T_c], \tag{2.1}$$

where f_c is the carrier (center) frequency, B is the bandwidth, T_c is the chirp duration and β defines the ramp rate. This LFM chirp is illustrated in frequency domain in Figure 2.1.

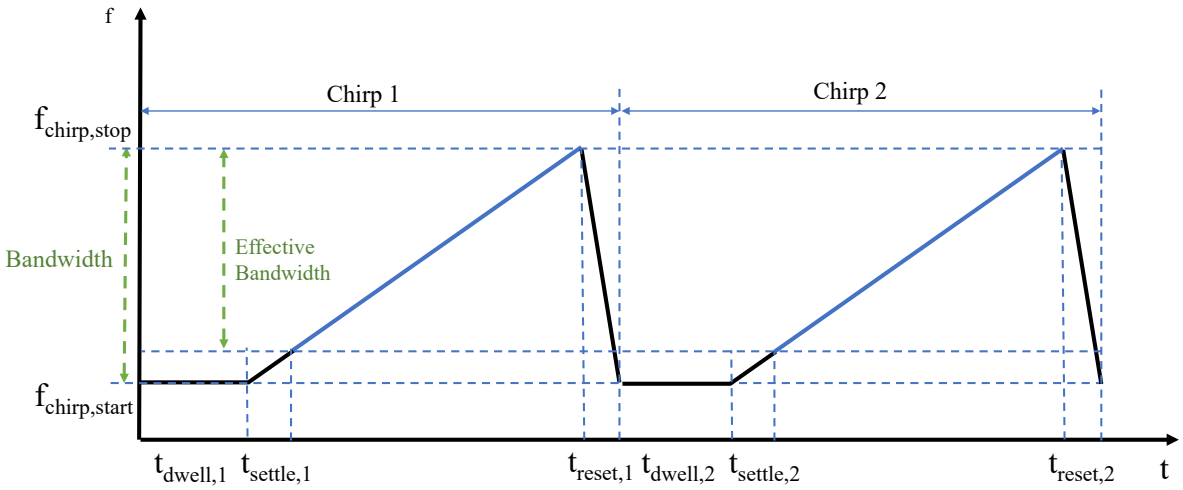

Figure 2.1: Chirp in frequency-time plot

Accordingly, the LFM sweep to be transmitted can be expressed as:

$$s_{Tx}(t) = h_{Tx} \cdot \exp\left(j2\pi \cdot \left(f_c t + \beta \frac{t^2}{2}\right)\right), \tag{2.2}$$

where h_{Tx} is the amplitude of the transmitted waveform.

When the transmitted signal illuminates the target, it reflects back to the receiver of the radar system. The received signal is a copy of the transmitted signal with certain delay $\tau(t)$ and complex amplitude h_{Rx}, proportional to the target radar cross-section (RCS), attenuation and pre-processing, which can be written as:

$$s_{Rx}(t) = h_{Rx} \cdot \exp\left(j2\pi \cdot \left(f_c(t-\tau(t)) + \beta\frac{(t-\tau(t))^2}{2}\right)\right). \tag{2.3}$$

Then, a process called deramping is applied to the received signal, which consist of mixing it with the transmitted signal and filtering out the high-frequency component, as demonstrated in Figure 2.2. The obtained signal is called beat signal and can be expressed as:

$$\begin{aligned} s_b(t) &= s_{Tx}(t) \cdot s^*_{Rx}(t) \\ &= h_b \cdot \exp\left(j2\pi \cdot \left(f_c\tau(t) + \beta\tau(t)t - \beta\frac{\tau(t)^2}{2}\right)\right), \end{aligned} \tag{2.4}$$

where $(\cdot)^*$ denotes the complex conjugate operation.

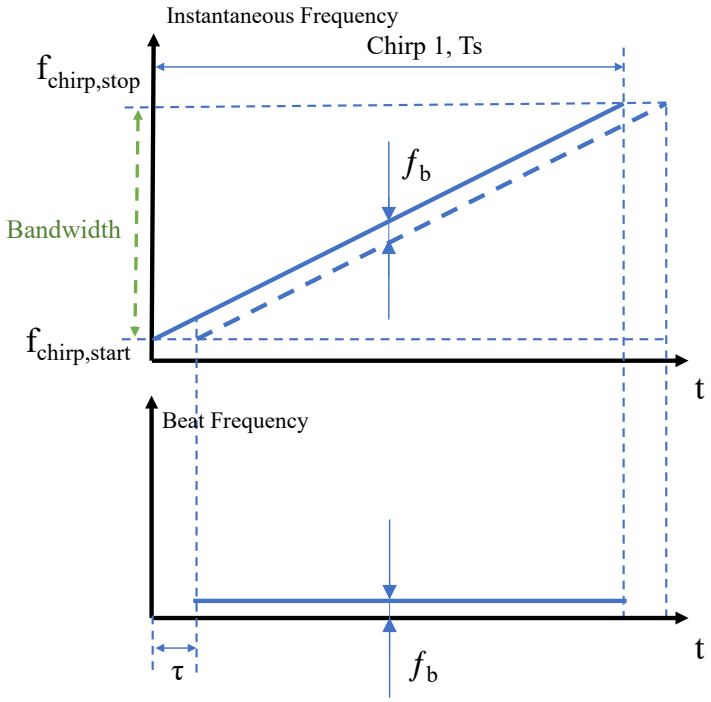

Figure 2.2: Deramping of LFM signal

The first term of the phase $2\pi f_c\tau(t)$ in (2.4) indicates the phase change over slow time and is called slow-time phase history while the third term $2\pi\beta\tau(t)^2/2$ is assumed negligible and thus it can be ignored [30].

For any point scatterer, the beat signal become a sinusoid with a frequency as inferred

from (2.4). This frequency is called beat frequency and is written as:

$$f_b = \beta\tau(t). \tag{2.5}$$

Applying Fourier transform to the beat signal in (2.4) over fast-time, the equation becomes:

$$S_b(f) = h_b T_c \cdot \exp\left(j2\pi \cdot f_c\tau(n)\right)\mathrm{sinc}\Big(T_c\left(f - \beta\tau(n)\right)\Big), \tag{2.6}$$

where $\mathrm{sinc}(x) = \sin(\pi x)/(\pi x)$ and n indicates the slow-time.

Assuming that the target is vibrating in range around a point at a distance R_0 and no range cell migration occurs, the delay $\tau(n)$ over slow-time can be written as:

$$\tau(n) = \frac{2\left(R_0 + \Delta R(n)\right)}{c}, \tag{2.7}$$

where $\Delta R(n)$ denotes the minor displacement of the target.

Substitute (2.7), (2.6) becomes:

$$\begin{aligned} S_b(f) &= h_b T_c \cdot \exp\left(j\frac{4\pi f_c}{c} \cdot \Big(R_0 + \Delta R(n)\Big)\right)\mathrm{sinc}\left(T_c\left(f - \beta\frac{2(R_0 - \Delta R(n))}{c}\right)\right) \\ &= h_b T_c \exp\left(\frac{4\pi f_c}{c}R_0\right)\exp\left(j\frac{4\pi f_c}{c} \cdot \Delta R(n)\right)\mathrm{sinc}\left(T_c\left(f - \beta\frac{2(R_0 - \Delta R(n))}{c}\right)\right). \end{aligned} \tag{2.8}$$

With no range cell migration assumption, (2.8) can be approximated with:

$$S_b(f) \approx h_b T_c \exp\left(\frac{4\pi f_c}{c}R_0\right)\exp\left(j\frac{4\pi f_c}{c} \cdot \Delta R(n)\right)\mathrm{sinc}\left(T_c\left(f - \beta\frac{2R_0}{c}\right)\right). \tag{2.9}$$

Then, the beat frequency becomes:

$$f_b \approx \beta\frac{2R_0}{c}. \tag{2.10}$$

Therefore, the range of the target can be estimated from beat frequency as:

$$R_0 = \frac{cf_b}{2\beta}. \tag{2.11}$$

Since the width of the main beam of the sinc function in (2.6) is:

$$T_c\frac{2\beta}{c} = \frac{c}{2B},$$

the range resolution is determined as:

$$\Delta R = \frac{c}{2B}. \tag{2.12}$$

2.2. Physiology of Cardiopulmonary Activity

In this section, the basic physiology of cardiopulmonary activity is briefly explained. With our main aim to estimate the frequency and amplitude of both breathing and heartbeat, it is common to model them as independent activities regardless of the relationship existing between them.

2.2.1. Heart Beat

Heart beat or cardiac cycle consists of two main periods. One is called diastole when heart muscle relaxes to refill venous blood and the other one coming behind is called systole with contraction of the heart muscle to pump blood into arteries. Traditional methods to detect the activity of heart beat is to measure the potentials induced by the heart electrical currents on the surface of prothorax as shown in Figure 2.3. The record of these potentals is referred as electrocardiogram (ECG).

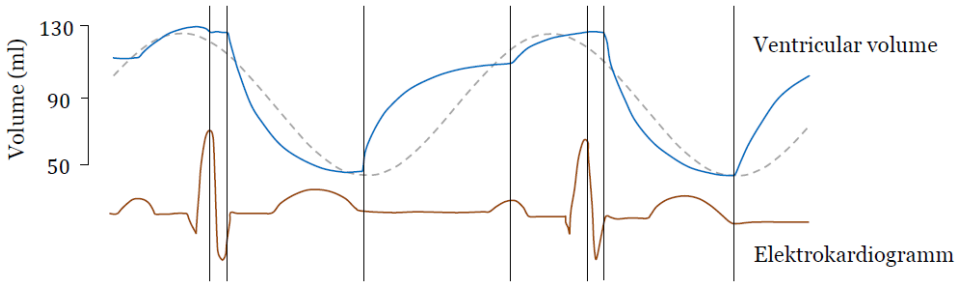

Figure 2.3: The electrocardiogram and changes in ventricular volume of cardiac cycles with sinusoidal approximation in dashed line [31].

Since an electromagnetic wave of frequency 77GHz will attenuate within the layer of skin, the measurement of heartbeat with radar is based on the physical motion caused by heart muscles rather than those muscles themselves. As a result, detection of a heartbeat corresponds to detecting the vibration of the left side of the prothorax exactly above the location of the heart and its muscles.

For a healthy adult, the typical heart rate is from 60 to 100 beats per minute, or equivalently from 1 to 1.667 Hz. The typical displacement of prothorax induced by heart muscles is ranging from 0.3 to 0.8 mm [13].

Since the focus of the project is to estimate the frequency and amplitude of the heart beat movement of the surface skin on chest, it is enough to estimate those parameters from the first order of the Fourier expansion of the real motion, *i.e.*, the sinusoid with the

heartbeat frequency. Therefore, for simplicity, the movement of the surface of prothroax due to heart beat can be modelled as a sinusoidal displacement:

$$R_h(t) \approx \alpha_h \cdot \sin(2\pi f_h \cdot t + \varphi_h). \tag{2.13}$$

Another two alternatives to model chest movement caused by heartbeat are $|\sin|$ and $(\sin)^3$ [32], which can be expressed as:

$$\begin{aligned} R_h(t) &\approx \alpha_h \cdot \sin|2\pi f_h \cdot t + \varphi_h|, \\ R_h(t) &\approx \alpha_h \cdot \sin^3(2\pi f_h \cdot t + \varphi_h). \end{aligned} \tag{2.14}$$

2.2.2. Respiration

The respiratory system is vital to human beings which provides the tissues of the human body with oxygen and clears the blood of the gaseous waste product like carbon dioxide. In order to finish this gas exchange, a complete breathing cycle has two main motions, inspiration and expiration. These activities are mainly completed by the responsible organ of lung located in the thorax. Lung expansion leads to inhalation and lung contraction corresponds to exhalation. Thanks to changes of lung volume caused by respiratory muscles, including diaphragm and certain intercostal muscles, prothorax moves accordingly as well as the chest cavity as shown in Figure 2.4.

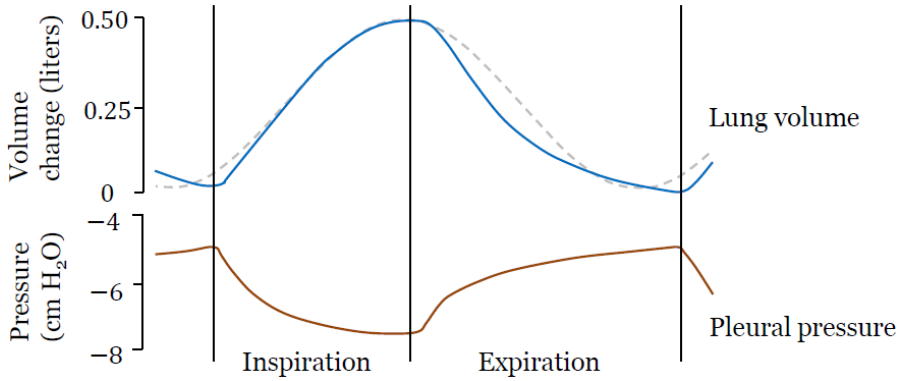

Figure 2.4: Changes in lung volume and pleural pressure during normal breathing [31]. (Sinusoidal approximation in dashed line.)

The prothorax movement due to respiratory activity then leads to the phase shift of reflected wave and can be detected by the radar.

For a healthy adult, the typical respiratory rate is from 6 to 20 breaths per minute. That is, respiratory rate is from 0.1 to 0.33 Hz. The typical displacement of prothorax induced by respiration is ranging from 3 to 11 mm [16].

Since the focus of the project is to estimate the frequency and amplitude of the respiratory movement of the surface on chest, it is enough to estimate those parameters

from the first order of the Fourier expansion of the real motion, *i.e.*, the sinusoidal mode with the same frequency as the real motion. Therefore, like the case of heartbeat, the movement of the skin of prothroax due to breathing activity can be modelled as a sinusoidal displacement as:

$$R_r(t) \approx \alpha_r \cdot \sin(2\pi f_r \cdot t + \varphi_r). \tag{2.15}$$

Like the movement modelling of heartbeat, chest movement caused by respiration can be modelled with two alternatives as $|\sin|$ and $(\sin)^3$ [32].

Vital signs	Frequency (Hz)	Amplitude (mm)
Respiration	[0.1, 0.33]	[3, 11]
Heartbeat	[1, 1.667]	[0.3, 0.8]

Table 2.1: Typical frequencies and amplitudes of vital signs

2.3. Radar Response of Vital Signs

With the basic physiology mentioned above, it is known that the detection for the motions of both respiration and heartbeat is based on the movement of the surface skin of prothroax. Therefore, considering the sin modelling for both vital signs, the position of the the surface skin of prothroax at a distance R_0 can be expressed as:

$$\begin{aligned} R(n) &= R_0 + R_r(n) + R_h(n) \\ &= R_0 + \alpha_r \cdot \sin(2\pi f_r \cdot n + \varphi_r) + \alpha_h \cdot \sin(2\pi f_h \cdot n + \varphi_h). \end{aligned} \tag{2.16}$$

Since the displacement of vital signs is only several millimeters and even down to sub-millimeters level and no range cell migration is assumed, phase history of the beat signal is very important to monitoring vital signs. Assuming that no variation of the human body back-scattering coefficient during the measurements, *i.e.*, h_b is constant in time, the phase history $\phi_{ph}(n)$ over slow-time as inferred from (2.9) can be written as:

$$\begin{aligned} \phi_{ph}(n) &= \frac{4\pi f_c}{c} \cdot R(n) \\ &= \frac{4\pi f_c}{c} \left(R_0 + \alpha_r \cdot \sin(2\pi f_r \cdot n + \varphi_r) + \alpha_h \cdot \sin(2\pi f_h \cdot n + \varphi_h)\right). \end{aligned} \tag{2.17}$$

Then, the range history over slow-time can be recovered from the phase history of beat signal:

$$R(n) = \frac{\phi_{ph}(n)c}{4\pi f_c}. \tag{2.18}$$

Therefore, in order to track the displacement of vital signs thus range history over slow-time, the preservation of the phase history is required which means that coherence maintenance of the radar system is necessary. Without coherence, only range profiles can be obtained but not phase information which is used to extract the information of target motion. This coherence maintenance does not only require the same waveform generation for each chirp but also require to preserve the clock shifts between the generation and data acquisition processes. As for the former one, the initial phase of each transmitted chirp, as indicated by upward arrows in Figure 2.5, must be constant. As for the latter one, the clock shifts must be constant and preserved and known such that there is no extra unknown phase variable in (2.18).

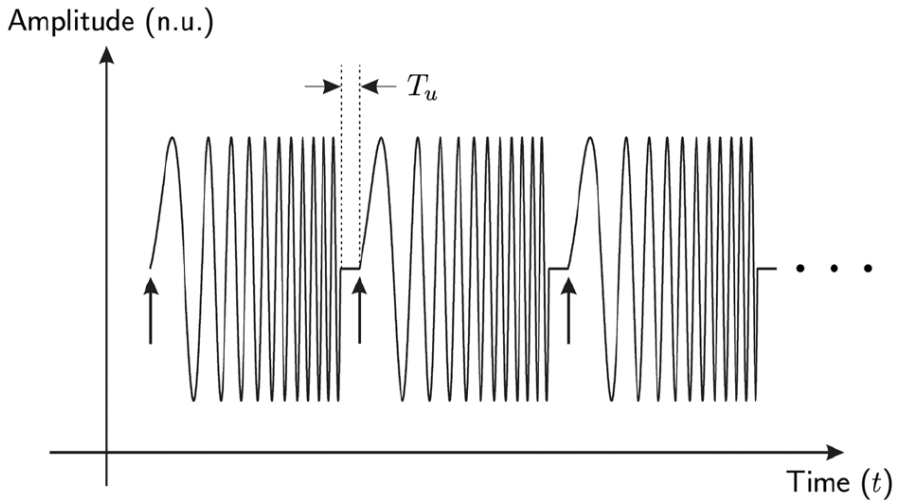

Figure 2.5: Phase control of each chirp

It should be noticed that although coherence is well preserved, the range R_0 can not be retrieved from (2.18) due to the wrapping of phase with its periodicity of 2π. Therefore, an extra phase ϕ_e occurs due to the wrapped phase caused by R_0:

$$\phi_e = \text{wrap}\left[\frac{4\pi f_c}{c} R_0\right], \tag{2.19}$$

where wrap[·] denotes the wrapping process of phase into interval $[0, 2\pi]$, which can be written as:

$$\text{wrap}[x] = \text{frac}\left(\frac{x}{2\pi}\right) \times 2\pi. \tag{2.20}$$

The phase history in (2.17) becomes:

$$\phi_{ph}(n) = \phi_e + \frac{4\pi f_c}{c}\left(\alpha_r \cdot \sin(2\pi f_r \cdot n + \varphi_r) + \alpha_h \cdot \sin(2\pi f_h \cdot n + \varphi_h)\right). \tag{2.21}$$

The maximal velocity of the weakest respiration activity is:

$$\begin{aligned} v_{r,min} &= \max\left\{\frac{\partial R_r(n)}{\partial t}\right\} \\ &= \max\left\{\alpha_{r,min}\cdot 2\pi f_{r,min}\cos(2\pi f_{r,min}n+\varphi_r)\right\} \\ &= \alpha_{r,min}\cdot 2\pi f_{r,min} \\ &= 1.9\times 10^{-3}[m/s]. \end{aligned}$$

The maximal velocity of the weakest heart activity is:

$$\begin{aligned} v_{h,min} &= \max\left\{\frac{\partial R_h(t)}{\partial t}\right\} \\ &= \max\left\{\alpha_{h,min}\cdot 2\pi f_{h,min}\cos(2\pi f_{h,min}t+\phi_{0,h})\right\} \\ &= \alpha_{h,min}\cdot 2\pi f_{h,min} \\ &= 1.9\times 10^{-3}[m/s]. \end{aligned}$$

The global maximal velocity of the weakest vital signs to be measured is:

$$v_{min} = \min\left\{v_{r,min}, v_{h,min}\right\} = 1.9\times 10^{-3}[m/s].$$

In order to be able to measure the maximal velocity of the weakest chest movement at $f_c = 77$ GHz, the required observation time T_d of the chirp train is:

$$\begin{aligned} \Delta v = \frac{c}{2T_d f_c} &\leq 10\%\cdot v_{min} \\ \Longrightarrow\ T_d &\geq 10\times\frac{c}{2f_c v_{min}} \\ &\geq 10\times\frac{3.0\times 10^8}{2\times 77\times 10^9\times 1.9\times 10^{-3}} \\ &\geq 10\times 1.0253 \\ &\geq 10.253[s]. \end{aligned}$$

Therefore, the required measurement time T_d is at least 10.253 s and the coherent processing interval (CPI) of 12 s is selected.

Considering only respiration activity and its sinusoidal model, the signal in the range cell including R_0 over slow-time can be written as:

$$s(n) = h\exp\left(j\phi_e\right)\exp\left(j\frac{4\pi f_c}{c}\left(\alpha_r\cdot\sin(2\pi f_r\cdot n+\varphi_r)\right)\right), \tag{2.22}$$

where h is the amplitude of the processed signal.

The power spectrum of the phase history in the signal $s(n)$ is shown in Figure 2.6, within which only one frequency peak of 0.2 Hz is observed and corresponds to the frequency of respiration $f_r = 0.2$ Hz.

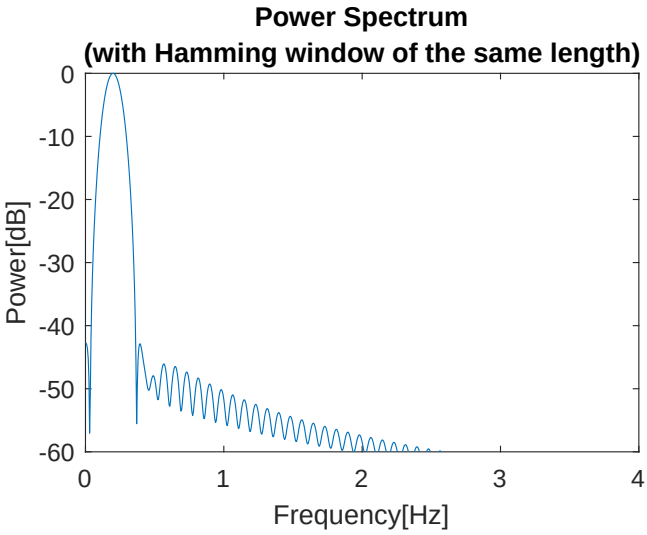

Figure 2.6: Doppler spectrum of the phase history in the signal $s(n)$ (Model: sin, $f_r = 0.2$ Hz)

Then, for a respiration movement with its amplitude $\alpha_r = 5$ mm, frequency $f_r = 0.2$ Hz and initial phase $\varphi_r = 0$, its spectrogram is shown in Figure 2.7a and the corresponding Doppler spectrum is shown in Figure 2.7b.

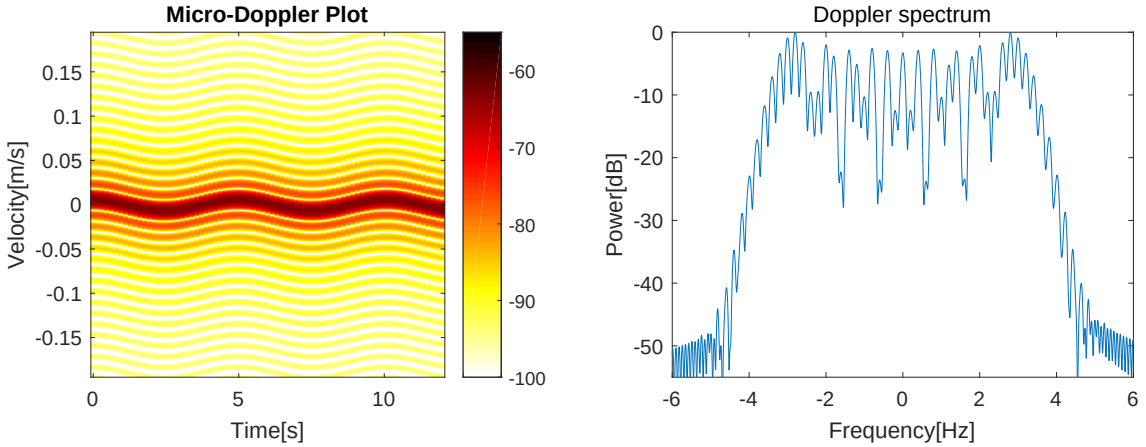

(a) Micro-Doppler

(b) Doppler spectrum

Figure 2.7: Micro Doppler and Doppler spectrum of the signal $s(n)$ (Model: sin, $\alpha_r = 5$ mm, $f_r = 0.2$ Hz and $\varphi_r = 0$)

From Figure 2.7a, it is observed that the micro-Doppler of the measured data monitoring respiration follows a sinusoidal wave. The Doppler spectrum of this signal $s(n)$ in Figure 2.7b shows that the signal energy spreads over the frequency interval

of $[-\frac{4\pi f_c}{c} a_r f_r, \frac{4\pi f_c}{c} a_r f_r] = [-3.23, 3.23]$ Hz due to the constantly changing velocity of the chest movement caused by respiration.

Ambiguity function of the breathing activity id defined as the cross correlation between the test signal and the reference signal:

$$C\left[(\alpha_r, f_r, \varphi_r), (\alpha_{ref}, f_{ref}, \varphi_{ref})\right] = \left| \int s_{a_r, f_r, \varphi_r}(n) s^*_{a_{ref}, f_{ref}, \varphi_{ref}}(n)\, dn \right|^2. \tag{2.23}$$

An example of such ambiguity function for $\alpha_{ref} = 5$ mm, $f_{ref} = 0.2$ Hz and $\varphi_{ref} = 0$ is shown in Figure 2.8. It is found that the maximum power of the secondary maxima is -6.727 dB lower than the main peak.

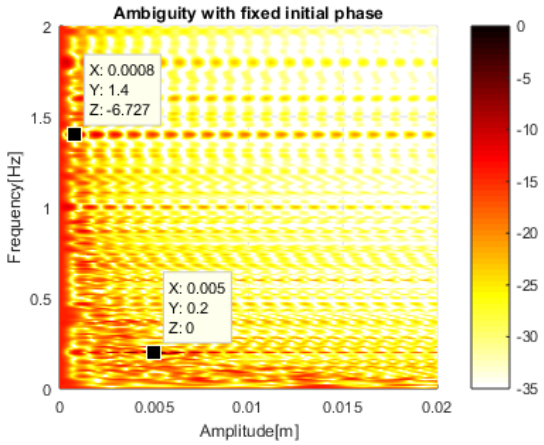

(a) Fixed initial phase

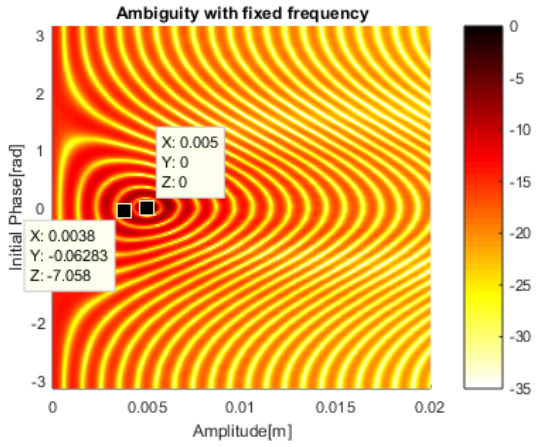

(b) Fixed frequency

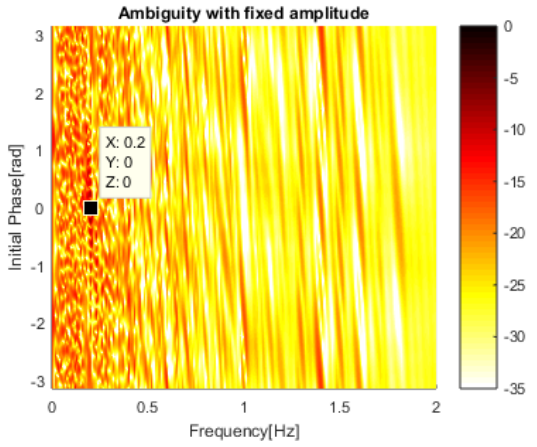

(c) Fixed amplitude

Figure 2.8: Ambiguity surface (Model: sin, $\alpha_{ref} = 5$ mm, $f_{ref} = 0.2$ Hz and $\varphi_{ref} = 0$)

The value of CPI will influence the performance of ambiguity function. For different CPIs of 6 s, 12 s and 24 s, the cut of ambiguity function over frequency f_r for fixed amplitude $\alpha_r = 5$ mm and fixed initial phase $\varphi_r = 0$ is shown in Figure 2.9.

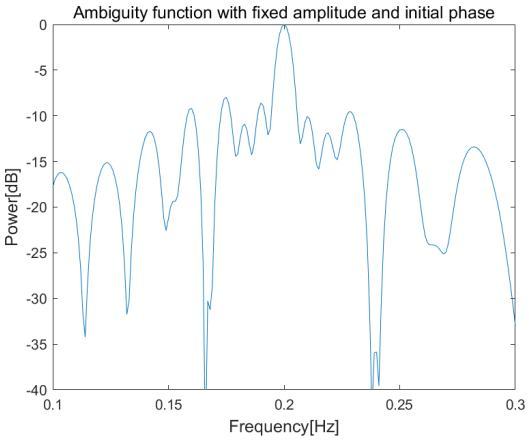

(a) CPI=6 s

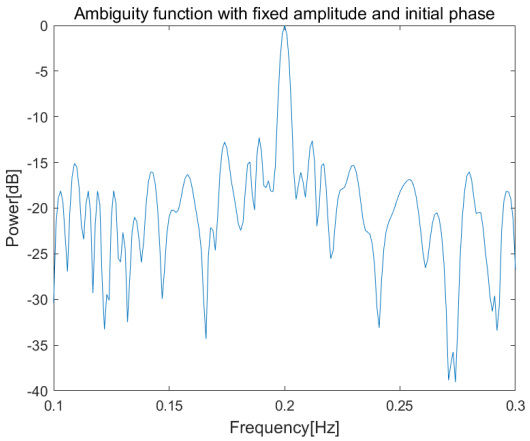

(b) CPI=12 s

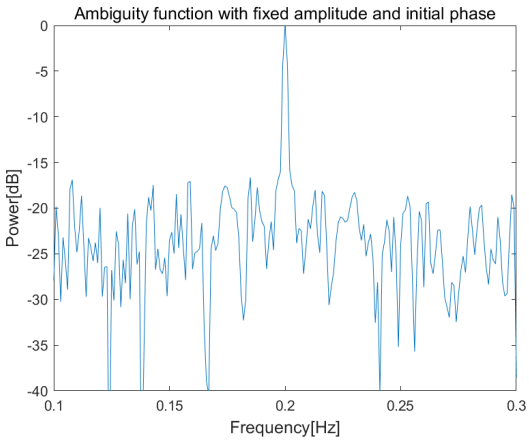

(c) CPI=24 s

Figure 2.9: Ambiguity function w.r.t. frequency with fixed amplitude $\alpha_r = 5$ mm and fixed initial phase $\varphi_r = 0$ (Model: sin, $f_{ref} = 0.2$ Hz)

It is shown in 2.9 that the frequency resolution becomes better as CPI increases. Meanwhile, the sidelobe level is lower with higher CPI.

If respiration activity is modelled as $|\sin|$ shape, the signal in the range cell including R_0 over slow-time becomes:

$$s(n) = h \exp(j\phi_e) \exp\left(j \frac{4\pi f_c}{c} (\alpha_r \cdot |\sin(2\pi f_r \cdot n + \varphi_r)|)\right). \tag{2.24}$$

The Doppler spectrum of this signal $s(n)$ is shown in Figure 2.10.

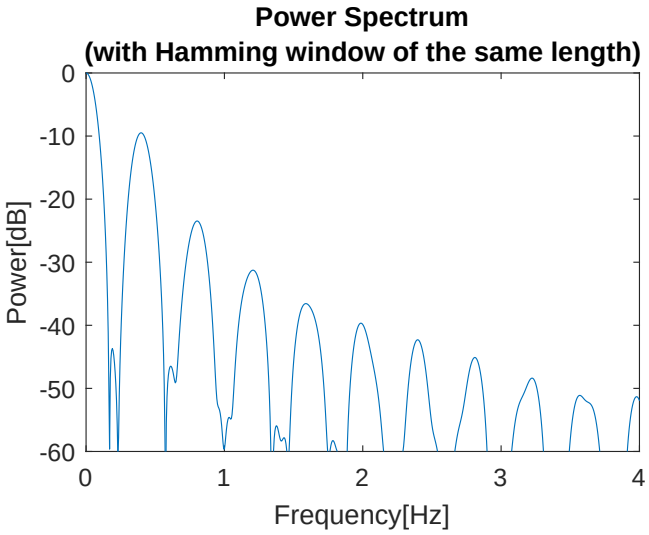

Figure 2.10: Doppler spectrum of the signal $s(n)$ (Model: $|\sin|$, $f_r = 0.2$ Hz)

It is observed from Figure 2.10 that those local peaks in the Doppler spectrum are corresponding to the Fourier series of $|\sin|$.

Then, its spectrogram is shown in Figure 2.11a and the corresponding Doppler spectrum is shown in Figure 2.11b.

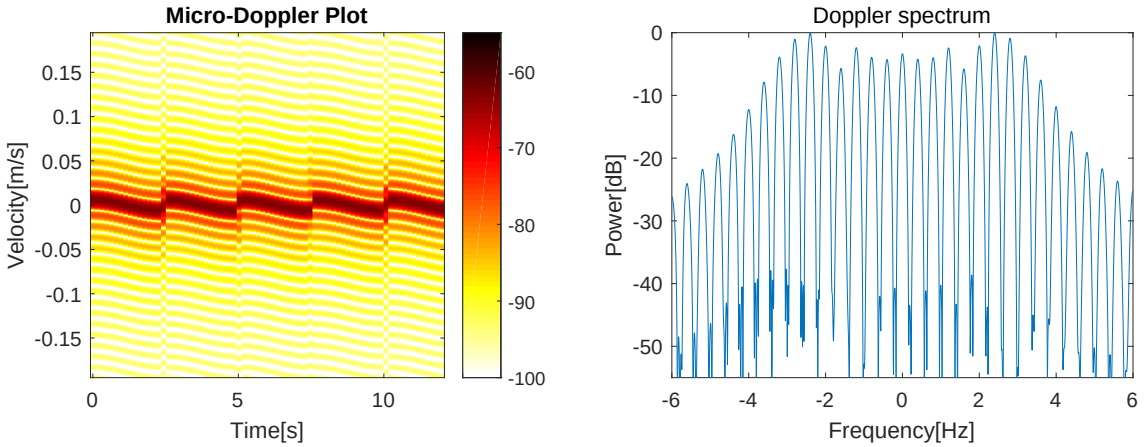

(a) Micro-Doppler

(b) Doppler spectrum

Figure 2.11: Micro Doppler and Doppler spectrum of the signal $s(n)$ (Model: $|\sin|$, $\alpha_r = 5$ mm, $f_r = 0.2$ Hz and $\varphi_r = 0$)

Its corresponding ambiguity function is shown in Figure 2.12.

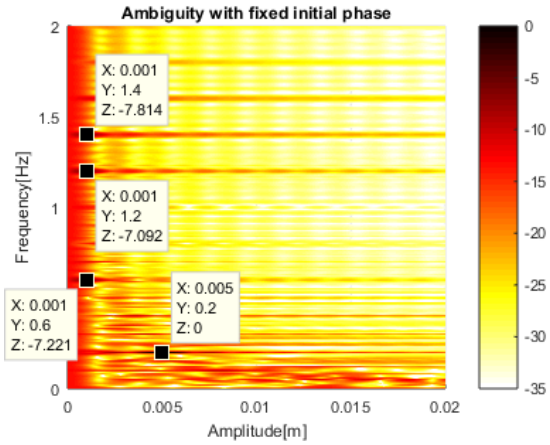

(a) Ambiguity with fixed initial phase

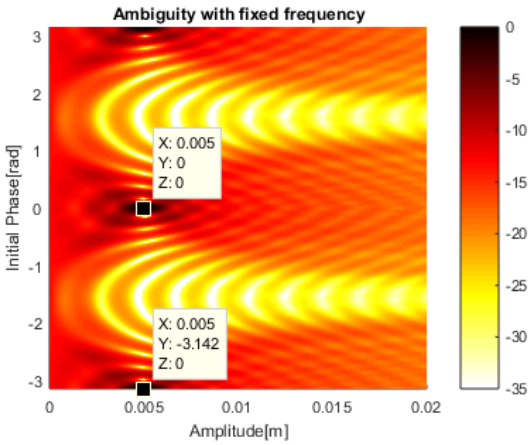

(b) Ambiguity with fixed frequency

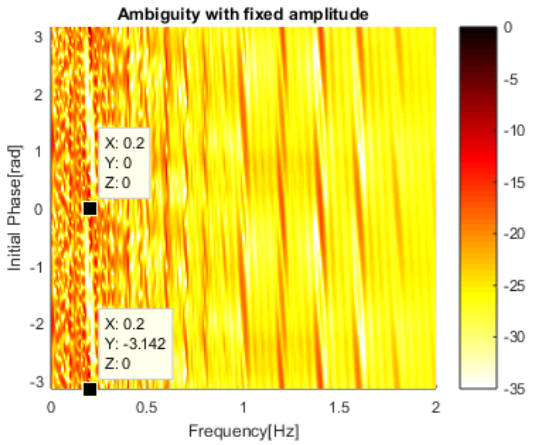

(c) Ambiguity with gixed amplitude

Figure 2.12: Ambiguity surface (Model: |sin|, $\alpha_{ref} = 5$ mm, $f_{ref} = 0.2$ Hz and $\varphi_{ref} = 0$)

From Figure 2.12, observation can be made that the maximum power of the secondary maxima is -7.092 dB lower than the main peak and artifacts occurs due to the reduced periodicity of |sin| function to be π. In addition, the curve of the spectrogram is not continuous changing due to the sudden change of curvature of |sin| shape at zeros.

The respiration activity can also be modelled as $(\sin)^3$ shape [32], the signal in the range cell including R_0 over slow-time becomes:

$$s(n) = h \exp(j\phi_e) \exp\left(j \frac{4\pi f_c}{c} \left(\alpha_r \cdot \sin^3(2\pi f_r \cdot n + \varphi_r)\right)\right). \tag{2.25}$$

The Doppler spectrum of this signal $s(n)$ is shown in Figure 2.13.

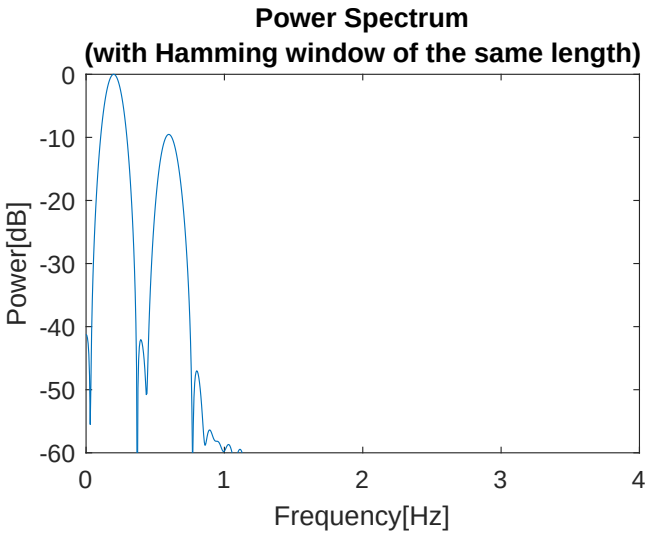

Figure 2.13: Doppler spectrum of the signal $s(n)$ (Model: $(\sin)^3$, $f_r = 0.2$ Hz)

It is observed that there are two peaks in the Doppler spectrum, 0.2 Hz and 0.6 Hz in Figure 2.13, which is corresponding to the Fourier series of $(\sin)^3$. The spectrogram of that model is shown in Figure 2.14a and the corresponding Doppler spectrum is presented in Figure 2.14b.

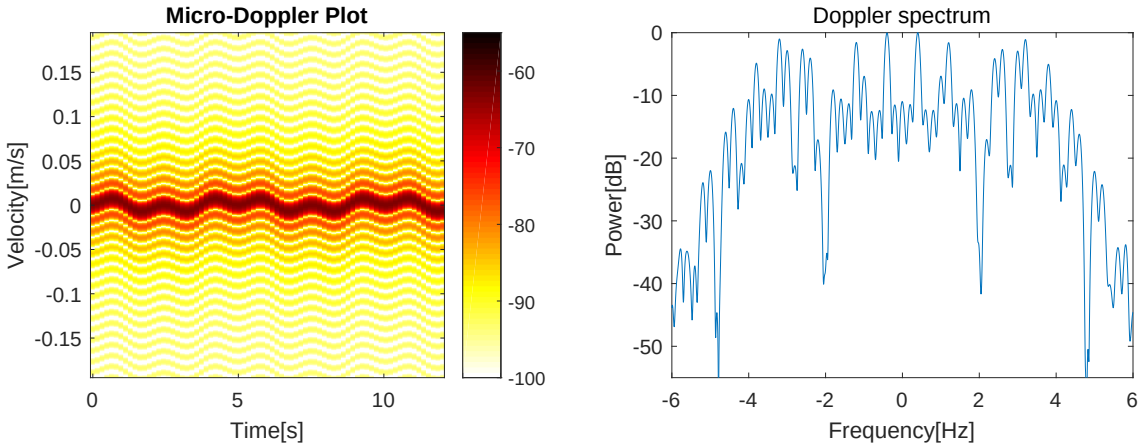

(a) Micro-Doppler

(b) Doppler spectrum

Figure 2.14: Micro Doppler and Doppler spectrum of the signal $s(n)$ (Model: $(\sin)^3$, $\alpha_r = 5$ mm, $f_r = 0.2$ Hz and $\varphi_r = 0$)

Its ambiguity are shown in Figure 2.15.

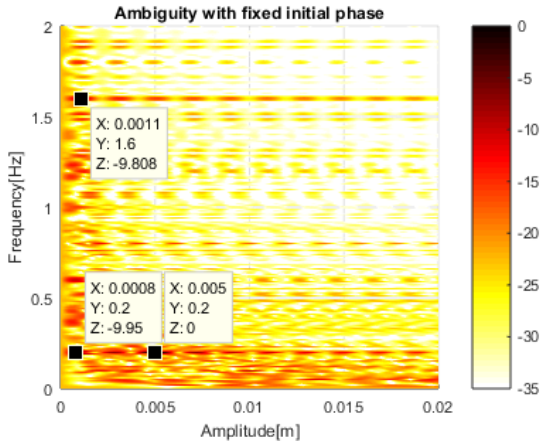

(a) Ambiguity with fixed initial phase

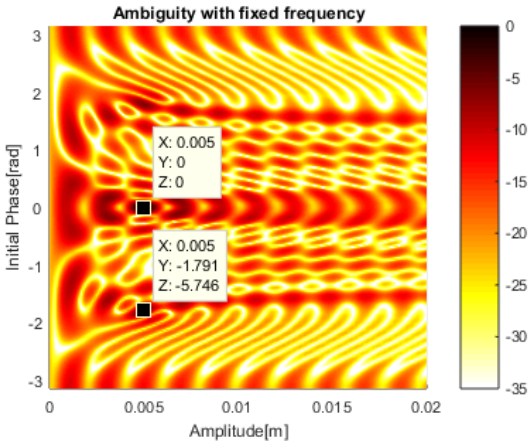

(b) Ambiguity with fixed frequency

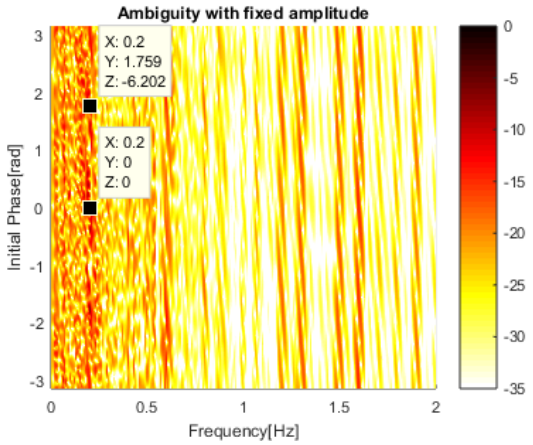

(c) Ambiguity with gixed amplitude

Figure 2.15: Ambiguity surface (Model: $(\sin)^3$, $\alpha_{ref} = 5$ mm, $f_{ref} = 0.2$ Hz and $\varphi_{ref} = 0$)

From Figure 2.15, it is observed that the maximum power of the secondary maxima is -5.746 dB lower than the main peak due to the shape of $(\sin)^3$ function. Like the model of sin, the curve of the spectrogram is continuous changing without any sudden change.

2.4. MIMO/Beamforming

In the application scenario in automobiles, the MIMO system is compulsory in order to focus focus the received power from a certain direction. In this way, clutter in the other directioncan be eliminated thus increasing SCR. Additionally, azimuth positioning can be achieved with a MIMO system which help radar localize the position of the target in 2D horizontally or in 3D domain. Therefore, different passengers in automotive can be separated.

2.5. Conclusion

In this Chapter, the basic physiology of the two vital signs – respiration and heartbeat – has been introduced. From this information, it is known that both heartbeat and respiration activities will lead to the change of the chest cavity, resulting in the motion of the surface of the skin on the prothroax.

Provided that the motion amplitudes of those vital signs are extremely small, radar technology is considered to detect and monitor the relative motion of the chest rather than the exact position of the chest surface. In addition, the power of possibly dynamic clutter (car vibration) has to be taken into consideration which can be relatively strong compared to the reflected signals from vital signs. Therefore, instead of using CW radar, LFMCW radar technology is considered. Benefiting from wider operational bandwidth, range of the target can be obtained with a good range resolution. By doing so, not only range information can be obtained, but also one can discriminate the desired signal from the unwanted signals in other range cells. As a result, the SCR is increased.

From the ambiguity analysis, it is found that the there is no artifact for frequency and amplitude estimation for different models of vital signs. The artifact occurred in initial phase domain is due to the shape thus periodicity of the model $|\sin|$. The sidelobe (false peak of ambiguity function) level is within $[-10, -5]$ dB for all models for CPI equal to 12 s. The frequency resolution becomes worse with the decrease of CPI.

By utilizing the spatial information or the structure information of the MIMO system, angular information of the target can be obtained. Based on the principle of the beamforming, MIMO system can increase the power of the desired signal while rejecting the clutter from other directions.

3

Vital Signs Parameters Estimation

The information of the vital signs is contained in the motion of the surface of the prothroax as has been shown in the previous chapter. Therefore, proper signal processing should be implemented to extract those information from the received signal.

The chapter starts by analyzing the variation of the received signal or its phase slow-time signal obtained in the last chapter. To perform the estimation to the phase history, the method of phase unwrapping is revised. Then, the dynamic model for the reflected signal and its phase history are provided. Dynamic estimation of vital signs parameters is addressed by applying extended Kalman filter and particle filter to the the data.

The performance of the proposed estimators is analysed in numerical simulations, presented in the next Chapter.

3.1. Extraction of Phase History

With well preserved coherence of the system the exact phase history over slow-time can be extracted with the algorithm presented in this section. Since the phase information is contained in the exponential term in (2.6), the algorithm is designed to transform the data into the desired form. Then, phase unwrapping processing is applied on extraction of the phase history from which the range history is computed.

Assuming that beat signal sampled in each interval of each ramp are stacked in rows, then the matrix of raw data $\mathbf{D}[n,t](n = 1,2,...,N; t = 1,2,...,T)$ (N is the number of chirps over slow-time and T the number of samples per chirp over fast-time) is built. The derivation of range history is divided into the following steps [33]:

Step 1: Implement a fast Fourier Transformation (FFT) over each row of the $\mathbf{D}[n,t]$, resulting in the range-profile matrix denoted as $\mathbf{RP}[n,r]$.

Step 2: Select the desired range bin r_d within which the target is found. Denote this signal as $\mathbf{s}[n] = \mathbf{RP}[n, r_d]$.

Step 3: Extract the corresponding phase of the signal $\mathbf{s}[n]$ and unwrap it, obtaining the phase history $\phi[n]$ as shown in Figure 3.1.

Step 4: Calculate the estimation of the scatterer range history as $\hat{R}[n] = \frac{c \cdot \phi[n]}{4\pi f_c}$.

The assumption is made that the scatterer should remain within the same range bin during the entire measurement time or so-called coherent processing interval (CPI). It is enough to hold this assumption since the motion of vital signs has limited magnitude and is unlikely to migrate to another range bin.

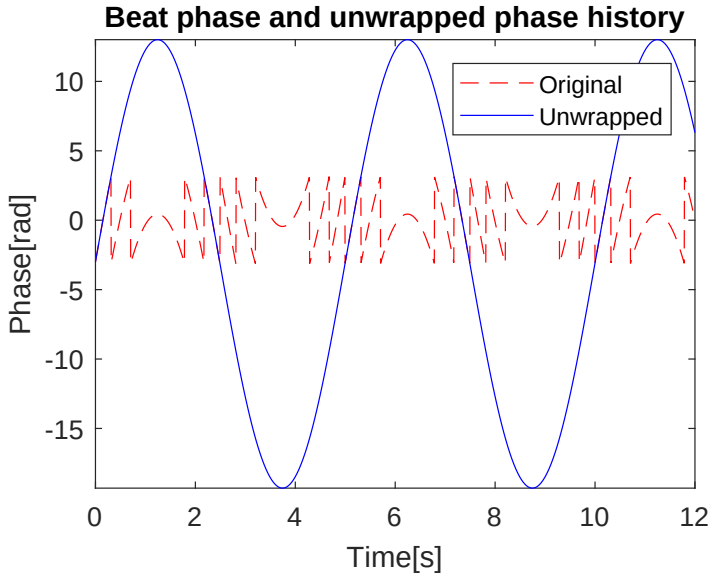

Figure 3.1: Phase history

It is noticeable that the phase change between any two consecutive ramps must not be less that 2π, *i.e.*, the range motion along the direction of light of sight (LOS) between any two consecutive chirp intervals should not exceed half of the wavelength of the center frequency. Otherwise the phase unwrapping will fail. The algorithm of phase unwrapping is listed as follows.

3.2. Dynamic Model

With the purpose to monitor vital signs and to estimate the characteristics of respiration and heartbeat, proper estimation method is considered. Instead of estimating those parameters from a long-term observation time, sequential estimator is used to be able to estimate and update the desired parameters from one sweep to another one. In the

Data: Input data
t_d is the desired range bin;
$\mathbf{s}[n] = \mathbf{RP}[n, t_d]$ (Range-profile matrix);
Result: Phase history $\phi[n] = \text{unwrap}(\text{angle}(\mathbf{s}[n]))$
begin
  $k = 0$;
  $\phi[n] = \text{angle}(\mathbf{s}[n])$;
  for $n = 1$ **to** $N - 1$ **do**
    $\phi[n+1] = \phi[n+1] + k \cdot 2\pi$;
    if $(\phi[n+1] - \phi[n]) > \pi$ **then**
      $\phi[n+1] = \phi[n+1] - 2\pi$;
      $k = k - 1$;
    end
    if $(\phi[n+1] - \phi[n]) < -\pi$ **then**
      $\phi[n+1] = \phi[n+1] + 2\pi$;
      $k = k + 1$;
    end
  end
end

Algorithm 1: Phase unwrapping with Matlab syntax

following, filter, as the term suggests, is used to extract the required information out from the received data.

In this section, several sequential filters are described respectively, based on the structure of the received data. By analyzing the structure of the received data and combining (2.9) and (2.16), the received data can be written as:

$$y(n) = h\exp\left(j\phi_e\right)\cdot\exp\left(j\frac{4\pi f_c}{c}\cdot\left(\alpha_r\cdot\sin(2\pi f_r\cdot n+\varphi_r)+\alpha_h\cdot\sin(2\pi f_h\cdot n+\varphi_h)\right)\right)+u, \quad (3.1)$$

where h is the amplitude of the signal, ϕ_R is the extra phase related to both range and property of scatterer and u is the assumed zero-mean, complex white Gaussian denoted as $u \sim \mathcal{CN}(0, \sigma_u^2)$. This equation is derived from (2.9) with a proper selected range bin, combined with the breathing model and heartbeat model in (2.16).

Nearly constant frequency (NCF) model is recalled [34] in this section and used to track the frequency and amplitude of a single-tone signal which corresponds to the unwrapped phase history provided that only respiration or only heartbeat of the human is considered. Model in real value is processed first to show the application of Kalman filter. Then, we turn to more complicated case of observing the signal in complex domain with complex Gaussian noise.

For simplicity, the signal model to be tracked is focused only on breathing activity

in this section. Inferred to (3.1), the signal becomes:

$$y(n) = h \exp\left(j\phi_e\right) \cdot \exp\left(j\frac{4\pi f_c}{c} \cdot \left(\alpha_r \cdot \sin(2\pi f_r \cdot n + \varphi_r)\right)\right) + u. \tag{3.2}$$

3.2.1. Baseband Signal

Assuming that noise for the complex signal in (3.2) is complex Gaussian noise and its real and imaginary parts are mutually independent, both real and imaginary parts are Gaussian. Therefore, intuitively, one option for the estimation can be based on in-phase and quadrature parts of the complex signal.

Instead of estimating frequency w_t and phase ϕ_t simultaneously, it is proposed to estimate the angle $\theta_t = w_t \cdot t + \phi_t$. Applying Taylor series expansion to θ_t and its first derivatives $\dot{\theta}_t = \frac{\partial \theta_t}{\partial t}$, the angle θ_t can written as:

$$\begin{aligned} \theta_t &\approx \theta(t - T_s) + T_s\dot{\theta}(t - T_s) + \frac{T_s^2}{2}\ddot{\theta}(t - T_s), \\ \dot{\theta}_t &\approx \dot{\theta}(t - T_s) + T_s\ddot{\theta}(t - T_s), \end{aligned} \tag{3.3}$$

where T_s is the sampling time or the pulse repetition interval. In addition, we assume that:

$$\begin{aligned} \dot{\theta}_t &= w_t \\ \ddot{\theta}_t &= \dot{w}_t \sim \mathcal{N}(0, \sigma_w^2) \end{aligned} \tag{3.4}$$

where σ_w^2 is the variance of the change of the frequency w_t. If the value of σ_w^2 is small enough, then w_t is slightly changed by the value of its counterpart at the previous time instant, w_{t-1}.

Similarly, we approximate the sinusoidal amplitude α_t as:

$$\begin{aligned} \alpha_t &\approx \alpha(t - T_s) + T_s\dot{\alpha}(t - T_s), \\ \dot{\alpha}_t &\sim \mathcal{N}(0, \sigma_\alpha^2). \end{aligned} \tag{3.5}$$

In this case, the state vector of the NCF model is given by:

$$\mathbf{x}_t = \begin{bmatrix} \theta_t \\ w_t \\ \alpha_t \\ h_t \\ \phi_{e,t} \end{bmatrix}. \tag{3.6}$$

With (3.3), (3.4) and (3.5), then state dynamic model is:

$$\begin{aligned}\mathbf{x}_t &= \mathbf{f}_m(\mathbf{x}_{t-1}) + \mathbf{B}_m\mathbf{v}_t \\ &= \mathbf{F}_m\mathbf{x}_{t-1} + \mathbf{B}_m\mathbf{v}_t,\end{aligned} \tag{3.7}$$

or written as:

$$\mathbf{x}_t = \begin{bmatrix} 1 & T_s & 0 & 0 & 0 \\ 0 & 1 & 0 & 0 & 0 \\ 0 & 0 & 1 & 0 & 0 \\ 0 & 0 & 0 & 1 & 0 \\ 0 & 0 & 0 & 0 & 1 \end{bmatrix} \begin{bmatrix} \theta_{t-1} \\ w_{t-1} \\ \alpha_{t-1} \\ h_{t-1} \\ \phi_{e,t-1} \end{bmatrix} + \begin{bmatrix} T_s^2/2 & 0 & 0 & 0 \\ T_s & 0 & 0 & 0 \\ 0 & T_s & 0 & 0 \\ 0 & 0 & 1 & 0 \\ 0 & 0 & 0 & 1 \end{bmatrix} \mathbf{v}_t, \tag{3.8}$$

where $\mathbf{v}_t = [v_{w,t}, v_{\alpha,t}, v_{h,t}, v_{\phi_e,t}]^T$ are the driving noises.

Then, since the amplitude α, frequency ω, magnitude h and extra phase ϕ_e are independent, their covariance matrix of their driving noises is:

$$\mathbf{Q} = \mathbb{E}\left\{\mathbf{v}_t\mathbf{v}_t^T\right\} = \begin{bmatrix} \sigma_w^2 & 0 & 0 & 0 \\ 0 & \sigma_\alpha^2 & 0 & 0 \\ 0 & 0 & \sigma_h^2 & 0 \\ 0 & 0 & 0 & \sigma_{\phi_e}^2 \end{bmatrix}. \tag{3.9}$$

With both real and imaginary parts of the signal, the observation model is:

$$\begin{aligned}\mathbf{y}_t &= \mathbf{g}_m(\mathbf{x}_t) + \mathbf{u}_t \\ &= \begin{bmatrix} x_{4,t}\cos\left(Cx_{3,t}\sin(x_{1,t}) + x_{5,t}\right) \\ x_{4,t}\sin\left(Cx_{3,t}\sin(x_{1,t}) + x_{5,t}\right) \end{bmatrix} + \begin{bmatrix} \mathrm{Re}(u_t) \\ \mathrm{Im}(u_t) \end{bmatrix},\end{aligned} \tag{3.10}$$

where $u_t = [\mathrm{Re}(u_t), \mathrm{Im}(u_t)]^T$ is the measurement noise for the real and imaginary part of the measured data. The measurement noise follows complex Gaussian noise assuming that the real and imaginary parts of the complex Gaussian noise are mutually independent thus the both parts of the noise follows the same real-valued Gaussian distribution with the same variance of $\frac{\sigma_u^2}{2}$. Then, the covariance is:

$$\mathbf{R} = \mathbb{E}\left\{\mathbf{u}_t\mathbf{u}_t^T\right\} = \begin{bmatrix} \frac{\sigma_u^2}{2} & 0 \\ 0 & \frac{\sigma_u^2}{2} \end{bmatrix}. \tag{3.11}$$

Perform linearization on the nonlinear observation function, the corresponding Jaco-

bian matrix is:

$$\mathbf{G}_{m,t} = \frac{\partial \mathbf{g}_m(\mathbf{x})}{\partial \mathbf{x}}|_{\mathbf{x}=\hat{\mathbf{x}}_{t|t-1}} = \\ = \hat{x}_{4,t|t-1} \cdot \begin{bmatrix} -QC\hat{x}_{3,t|t-1}\cos(\hat{x}_{1,t|t-1}) & 0 & -QC\sin(\hat{x}_{1,t|t-1}) & I/\hat{x}_{4,t|t-1} & -Q \\ IC\hat{x}_{3,t|t-1}\cos(\hat{x}_{1,t|t-1}) & 0 & IC\sin(\hat{x}_{1,t|t-1}) & Q/\hat{x}_{4,t|t-1} & I \end{bmatrix}, \tag{3.12}$$

where,

$$\begin{bmatrix} I \\ Q \end{bmatrix} = \begin{bmatrix} \cos\left(\hat{x}_{3,t|t-1}\sin(\hat{x}_{1,t|t-1}) + \hat{x}_{5,t|t-1}\right) \\ \sin\left(\hat{x}_{3,t|t-1}\sin(\hat{x}_{1,t|t-1}) + \hat{x}_{5,t|t-1}\right) \end{bmatrix}. \tag{3.13}$$

3.2.2. Phase History

Another option for the estimation of frequency f_r and amplitude α_r can be based on the unwrapped phase history of $\phi_{ph}(n)$ assuming that the noise in phase is Gaussian since there is no sidelobes within the ambiguity function for a sinusoidal wave. Further, there is only four unknowns under estimation in terms of phase history. From (3.2), the measured data is the unwrapped phase history $\phi_{ph}(n)$ in can be written as:

$$y_t = C \cdot \alpha_t \sin(w_t t + \varphi_t) + \theta_{av} + u_t, \tag{3.14}$$

where α_t, w_t and ϕ_t are the sinusoidal amplitude, frequency and phase, respectively. u_t is assumed to be an additive white Gaussian noise (AWGN) with zero mean and the constsnt scale factor:

$$C = \frac{4\pi f_c}{c}. \tag{3.15}$$

The average phase id denoted by θ_{av}, which is caused by the extra phase ϕ_e, the 2π wrapping effect of the phase history $\phi_{ph}(n)$ at start point of time as well as the reflection coefficient of the target, as shown in Figure 3.2.

It can be observed from Figure 3.2 that unwrapped phase history obtained from the phase of the beat signal is a sinusoidal wave, corresponding to the breathing sinusoidal model in (2.15) with a phase scaling factor constant C. An average phase is added to this unwrapped phase history. With the influence of complex noise, the average phase of the phase history can vary over time when the received pulses are of low SNR as shown in Figure 3.2b with $SNR_{pulse} = 6$ dB.

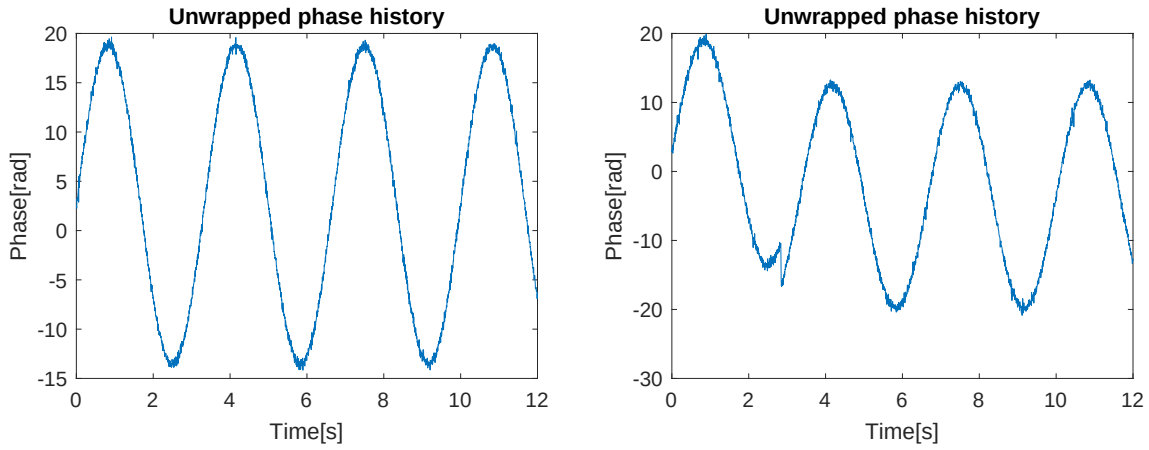

(a) $SNR_{pulse} = 8$ dB (b) $SNR_{pulse} = 6$ dB

Figure 3.2: Unwrapped phase history with different values of SNR_{pulse} ($\alpha_r = 5$ mm, $f_r = 0.3$ Hz and random φ_t)

Defining the state vector as:

$$\mathbf{x}_t = \begin{bmatrix} \theta_t \\ w_t \\ \alpha_t \\ \theta_{av} \end{bmatrix}. \tag{3.16}$$

With (3.3), (3.4) and (3.5), then state dynamic model is:

$$\begin{aligned} \mathbf{x}_t &= \mathbf{f}_m(\mathbf{x}_{t-1}) + \mathbf{B}_m \mathbf{v}_t \\ &= \mathbf{F}_m \mathbf{x}_{t-1} + \mathbf{B}_m \mathbf{v}_t, \end{aligned} \tag{3.17}$$

or written as:

$$\begin{bmatrix} \theta_t \\ w_t \\ \alpha_t \\ \theta_{av,t} \end{bmatrix} = \begin{bmatrix} 1 & T_s & 0 & 0 \\ 0 & 1 & 0 & 0 \\ 0 & 0 & 1 & 0 \\ 0 & 0 & 0 & 1 \end{bmatrix} \begin{bmatrix} \theta_{t-1} \\ w_{t-1} \\ \alpha_{t-1} \\ \theta_{av,t-1} \end{bmatrix} + \begin{bmatrix} T_s^2/2 & 0 & 0 \\ T_s & 0 & 0 \\ 0 & T_s & 0 \\ 0 & 0 & 1 \end{bmatrix} \mathbf{v}_t, \tag{3.18}$$

where $\mathbf{v}_t = [v_{w,t}, v_{\alpha,t}, v_{\theta_{av},t}]^T$ are the driving noises. With constant $\mathbf{F}_m$ over time, the evolution function $\mathbf{f}_m$ of state $\mathbf{x}_t$ is linear with NCF model.

Since the amplitude and frequency are independent, the covariance matrix of their driving noises is:

$$\mathbf{Q} = \mathbb{E}\left\{\mathbf{v}_t \mathbf{v}_t^T\right\} = \begin{bmatrix} \sigma_w^2 & 0 & 0 \\ 0 & \sigma_\alpha^2 & 0 \\ 0 & 0 & \sigma_{\theta_{av}}^2 \end{bmatrix}. \tag{3.19}$$

The observation model is:

$$y(t) = \mathbf{g}_m(\mathbf{x}_t) + u_t = C \cdot x_{3,t} \sin(x_{1,t}) + x_{4,t} + u_t. \tag{3.20}$$

Since the observation function $\mathbf{g}_m$ is nonlinear, linearization of the function can be approximated by take its first order of Taylor expansion. The corresponding Jacobian matrix is:

$$\mathbf{G}_{m,t} = \frac{\partial \mathbf{g}_m(\mathbf{x})}{\partial \mathbf{x}}|_{\mathbf{x}=\hat{\mathbf{x}}_{t|t-1}} = \begin{bmatrix} C \cdot \hat{x}_{3,t|t-1} \cos(\hat{x}_{1,t|t-1}) & 0 & C \cdot \sin(\hat{x}_{1,t|t-1}) & \hat{x}_{4,t|t-1} \end{bmatrix}. \tag{3.21}$$

The covariance matrix of the observation noise is:

$$\mathbf{R} = \mathbb{E}\left\{\mathbf{u}_t \mathbf{u}_t^T\right\} = \begin{bmatrix} \sigma_u^2 \end{bmatrix}. \tag{3.22}$$

3.3. Extended Kalman Filter

Kalman filter, known as linear quadratic estimation, is an optimal minimum mean square error (MMSE) estimator if the signal and noise are jointly Gaussian. Otherwise, it is the optimal linear minimum mean square error (LMMSE) estimator. However, the Kalman filter is originated for linear problems. As the motion of vital signs is nonlinear, an approximate solution is to linearize the state and/or observation function which are nonlinear. This results in a subsequent application of the Kalman filter for linear case, which is called extended Kalman filter (EKF). Since it is based on the linearization approximation of the original nonlinear model, there is no guarantee for the optimality [35].

In the discrete domain, Kalman filter definition in terms of state space is helpful to simplify the implementation of the filter.

Assume that we have the state evolution of the form,

$$\mathbf{x}_t = \mathbf{f}_m(\mathbf{x}_{t-1}) + \mathbf{B}_m \mathbf{v}_t, \tag{3.23}$$

where the subscript m indicates the given model and the subscript t indicates the time instant, $\mathbf{f}_m(\cdot)$ is the evolution function of the state which can be linear or nonlinear and $\mathbf{B}_m$ is the given matrix for the model. $\mathbf{v}_t \in \mathbb{R}^{n_v}$ refers to the driving noise vector with the same number of components as the state vector $\mathbf{x}_t \in \mathbb{R}^{n_x}$ and each component is a zero-mean, white Gaussian random variable. $\mathbf{Q} \in \mathbb{R}^{n_v \times n_v}$ is the covariance matrix of the driving noise and $\mathbf{Q} = \mathbb{E}\left\{\mathbf{v}_t \mathbf{v}_t^T\right\}$.

Then, the observation model is:

$$\mathbf{y}_t = \mathbf{g}_m(\mathbf{x}_t) + \mathbf{u}_t, \tag{3.24}$$

where the observation function $\mathbf{g}_m(\cdot)$ could be either linear or nonlinear and $\mathbf{u}_t$ is the measurement noise of the data vector $\mathbf{y}_t$ at time t with its covariance matrix $\mathbf{R} \in \mathbb{R}^{n_u \times n_u}$ known and $\mathbf{R} = \mathbb{E}\left\{\mathbf{u}_t \mathbf{u}_t^T\right\}$.

If either the evolution function $\mathbf{f}_m(\cdot)$ or the observation function $\mathbf{g}_m(\cdot)$ is nonlinear, then taking the linearization form of these function by taking the first order of their Taylor series expansion and Kalman filter is extended to the domain of nonlinear function when the models are weakly nonlinear and non-Gaussian.

The extended Kalman filter (EKF) evaluates

$$\begin{aligned}
\textbf{State Prediction:} \quad & \hat{\mathbf{x}}_{t|t-1} = \mathbf{f}_m(\hat{\mathbf{x}}_{t-1|t-1}) \\
\textbf{Covariance Prediction:} \quad & \mathbf{P}_{t|t-1} = \mathbf{F}_{m,t}\mathbf{P}_{t-1|t-1}\mathbf{F}_{m,t}^T + \mathbf{B}_m\mathbf{Q}\mathbf{B}_m^T \\
\textbf{Kalman Gain:} \quad & \mathbf{K}_t = \mathbf{P}_{t|t-1}\mathbf{G}_{m,t}^T(\mathbf{G}_{m,t}\mathbf{P}_{t|t-1}\mathbf{G}_{m,t}^T + \mathbf{R})^{-1} \\
\textbf{Update Estimation:} \quad & \hat{\mathbf{x}}_{t|t} = \hat{\mathbf{x}}_{t|t-1} + \mathbf{K}_t\Big(\mathbf{y}_t - \mathbf{g}_m(\hat{\mathbf{x}}_{t|t-1})\Big) \\
\textbf{Update Covariance:} \quad & \mathbf{P}_{t|t} = \Big(\mathbf{I} - \mathbf{K}_t\mathbf{G}_{m,t}\Big)\mathbf{P}_{t|t-1}
\end{aligned} \tag{3.25}$$

where $\mathbf{F}_{m,t}$ and $\mathbf{G}_{m,t}$ are the corresponding Jacobian matrix of the $\mathbf{f}_m$ and $\mathbf{g}_m$, respectively, which are

$$\begin{aligned}
\mathbf{F}_{m,t} &= \frac{\partial \mathbf{f}_m(\mathbf{x})}{\partial \mathbf{x}}|_{\mathbf{x}=\hat{\mathbf{x}}_{t-1|t-1}}, \\
\mathbf{G}_{m,t} &= \frac{\partial \mathbf{g}_m(\mathbf{x})}{\partial \mathbf{x}}|_{\mathbf{x}=\hat{\mathbf{x}}_{t|t-1}}.
\end{aligned} \tag{3.26}$$

3.4. Particle Filter

Although KF performs as optimal sequential estimator in linear Gaussian case, the models of the vital signs are nonlinear and the linearization extension of KF, referred to EKF, are also restricted the type of noise as Gaussian. However, the noise for the phase, the second exponential term in (3.1), is not Gaussian, since the noise u is Gaussian in complex domain but its magnitude and argument does not follow Gaussian distribution. If the real and imaginary part of the noise are mutual independent, then the magnitude of the complex random variable has a Rayleigh distribution and its argument will have a uniform distribution within $[-\pi, \pi]$.

Particle filter (PF), also as sequential Monte Carlo (SMC), is considered as a generalization form of KF with its advantage in solving filtering problem for nonlinear and/or

non-Gaussian signal-observation models as compared to KF, which is more suitable in the application of monitoring vital signs. Based on the simulated target distribution of each preset particle, the weight of each particle is computed and contributed as a measure of its respective importance. Those particles propagate and with update to be the next set of particles based on the updated importance. From a statistical point of view, importance sampling can be computed by maximum a posteriori (MAP), minimum mean square error (MMSE) estimation and etc.

At any time $(t-1)$, the posterior distribution function or importance distribution function $\pi(\mathbf{x}_{t-1}|\mathbf{y}_{1:t-1})$ can be approximated with N_p particles $\left\{\mathbf{x}_{t-1}^{(i)}\right\}_{i=1}^{N_p}$ and their corresponding weights $\left\{\mathbf{w}_{t-1}^{(i)}\right\}_{i=1}^{N_p}$ as:

$$\pi(\mathbf{x}_{t-1}|\mathbf{y}_{1:t-1}) \approx \sum_{i=1}^{N_p} \mathbf{w}_{t-1}^{(i)} \delta(\mathbf{x}_{t-1} - \mathbf{x}_{t-1}^{(i)}), \tag{3.27}$$

where the notion $(\cdot)_{1:t-1}$ indicates all the elements from time 1 to time $(t-1)$ and $\delta(\cdot)$ is the Dirac delta function. As the importance function can be written in an iterative form via:

$$\begin{aligned}\pi(\mathbf{x}_{0:t}|\mathbf{y}_{1:t}) &= \pi(\mathbf{x}_{0:t-1}|\mathbf{y}_{1:t-1})\pi(\mathbf{x}_t|\mathbf{x}_{0:t-1}, \mathbf{y}_{1:t}) \\ &= \pi(\mathbf{x}_0)\prod_{k=1}^{t}\pi(\mathbf{x}_k|\mathbf{x}_{0:k-1}, \mathbf{y}_{1:k}),\end{aligned}$$

from which one can evaluate the importance weights recursively in time:

$$\mathbf{w}_t^{(i)} \propto \mathbf{w}_{t-1}^{(i)} \times \frac{p(\mathbf{y}_t|\mathbf{x}_t^{(i)})p(\mathbf{x}_t^{(i)}|\mathbf{x}_{t-1}^{(i)})}{\pi(\mathbf{x}_t^{(i)}|\mathbf{x}_{0:t-1}^{(i)}, \mathbf{y}_{1:t})}, \tag{3.28}$$

where importance weights normalization should be implemented at the previous time $(t-1)$ as $\sum_{i=1}^{N_p} \mathbf{w}_{t-1}^{(i)} = 1$. The new set of particles $\left\{\mathbf{x}_t^{(i)}\right\}_{i=1}^{N_p}$ is generated from an properly chosen function (with notation $q(\cdot)$),

$$\mathbf{x}_t^{(i)} \sim q(\mathbf{x}_t|\mathbf{x}_{0:t-1}^{(i)}, \mathbf{y}_{1:t}), \tag{3.29}$$

which known as importance sampling function, minimizing the variance of the importance weights with the conditions on $\mathbf{x}_{0:t-1}^{(i)}$ and $\mathbf{y}_{1:t}$ [36].

If the prior distribution is assumed to be the importance distribution, then, we have,

$$\pi(\mathbf{x}_{0:t}|\mathbf{y}_{1:t}) = p(\mathbf{x}_{0:t}) = p(\mathbf{x}_0)\prod_{k=1}^{t} p(\mathbf{x}_k|\mathbf{x}_{k-1}),$$

and, the importance weights becomes,

$$\mathbf{w}_t^{(i)} \propto \mathbf{w}_{t-1}^{(i)} p\left(\mathbf{y}_t|\mathbf{x}_t^{(i)}\right), \tag{3.30}$$

which is a prevailing assumption to take in many applications of PFs.

Once the new set of particles $\mathbf{x}_t^{(i)}$ and their corresponding importance weights $\mathbf{w}_t^{(i)}$ are obtained, the estimation of the desired state can be made based on the prior knowledge with any estimations like MAP:

$$\begin{aligned}\hat{\mathbf{x}}_t &= \mathbb{E}\left[\mathbf{x}_t|\mathbf{y}_{1:t}\right] \\ &= \int \mathbf{x}_t \pi(\mathbf{x}_t|\mathbf{y}_{1:t})\, d\mathbf{y}_{1:t} \\ &\approx \sum_{i=1}^{N_p} \mathbf{w}_t^{(i)} \mathbf{x}_t^{(i)},\end{aligned} \tag{3.31}$$

where the notation $\mathbb{E}$ stands for expectation.

An attractive way to do is that new particles will be regenerated while only updating the importance weights recursively. This method is known as sequential importance sampling (SIS). However, the problem existed in SIS method is that, the distribution of the importance weights $\mathbf{w}_t^{(i)}$ is gradually skewed as sequential estimator progressing [37]. Consequently, only few particles contribute to the final estimator with very large importance weights while the other particles contribute nothing with their importance weights close to zero. Thus, the performance of this algorithm leads to the problem of degeneracy.

In order to surmount the problem of degeneracy in SIS algorithm, methods of regenerating new set of particles at each iteration are considered. As (3.29) suggests, regeneration for a new set of particles is possible with proper chosen importance sampling function. However, the analytic form of this function is rarely found in practice. Therefore, it was proposed to use dynamic prior as the importance sampling function:

$$\mathbf{x}_t^{(i)} \sim q(\mathbf{x}_t|\mathbf{x}_{0:t-1}^{(i)}, \mathbf{y}_{1:t}) = p\left(\mathbf{x}_k|\mathbf{x}_{k-1}^{(i)}\right). \tag{3.32}$$

This method is known as the bootstrap filter [38]. The main idea of this filter is to duplicate the particles based on their high importance weights respectively to replace those particles with lower importance weights. As a result, the number of the particles with higher importance weights increases while that with lower importance weights decreases. After this sampling, all the new particles are regarded with equal importance weights for the next iteration. This kind of resampling are also referred as sequential importance resampling (SIR). The algorithm of the bootstrap filter is listed

as follows.

begin
  `Initialization:`
  `t = 0;`
  for $i = 1$ **to** N_p **do**
    `Generate particles:` $\mathbf{x}_0^{(i)} \sim p(\mathbf{x}_0)$;
  end
  $t = 1$;
  `Importance sampling:`
  for $t = 1$ **to** N **do**
    `State evolution:`
    for $i = 1$ **to** N_p **do**
      $\mathbf{x}_t^{(i)} \sim p(\mathbf{x}_t|\mathbf{x}_{t-1})$;
    end
    `Importance weights:`
    for $i = 1$ **to** N_p **do**
      $\mathbf{w}_t^{(i)} = p(\mathbf{y}_t|\mathbf{x}_t^i)$;
    end
    `Importance weights Normalization:` $\mathbf{w}_{norm,t}^{(i)} = \frac{\mathbf{w}_t^{(i)}}{\sum_{i=1}^{N_p} \mathbf{w}_t^{(i)}}$;
    `Resampling:` $\mathbf{x}_t^{(i)} \sim \mathbf{w}_{norm,t}^{(i)}$
  end
end

Algorithm 2: Bootstrap filter with Matlab syntax

3.5. Conclusion

In this chapter, estimation of the breathing activity from measured data is presented. With our assumption that the respiration is nearly constant during the observation time, the corresponding NCF dynamic model is introduced.

Assuming that measurement noise is complex Gaussian, Kalmain filter is introduced and EKF is described by linearizing the nonlinear observation model with 5 unknown parameters based on the I/Q demodulation of the measured data. Since the real and imaginary parts of complex Gaussian noise are assumed to be mutually independent, The noise for both the real and imaginary parts of the observation signal is real-valued Gaussian. For higher value of SNR_{pulse}, the phase noise is assumed to be Gaussian. By utilizing the unwrapped algorithm of the phase history, the observation model with 4 unknown parameters are presented. Then, the general algorithm of implementing EKF follows.

For more complex measurement model with non-Gaussian noise, particle filter is introduced which performs as the general form of KF. Basic idea of SIS and SIR algorithm is explained and the detailed algorithm of bootstrap filter is presented.

4

Simulation

In this chapter, simulations results of applying both EKF and PF to the vital signs are demonstrated. For simplicity, only respiration is considered to demonstrate the challenges of the estimation. The simulation results with the two estimation methods are shown and analyzed. After successful estimation of the respiration, simultaneous estimation of both vital signs is described.

The radar parameters for all the simulations presented were properly selected, as listed in Table 4.1.

Parameters	Values
Center Frequency	77 GHz
Bandwidth	150 MHz
PRF	200 Hz
CPI	12 s
Chirp Time	4.5 ms
Sampling Frequency	1 MHz

Table 4.1: Radar parameters for simulation

4.1. Estimation for Respiration Only

In this section, only breathing frequency is considered. Simulation results using EKF and PF for NCF model are presented and analyzed.

4.1.1. Extended Kalman Filter Based On I/Q Demodulation

With the breathing model as expressed in (2.22), initial trial of employing EKF is to demodulate the complex signal into real and imaginary parts. Then, with Gaussian distribution of both real and imaginary parts of the noise, the NCF model for this EKF estimator is shown in (3.6)-(3.13). With SNR for each pulse SNR_{pulse} equal to 5 dB, the real and imaginary parts of the signal are shown in Figure 4.1.

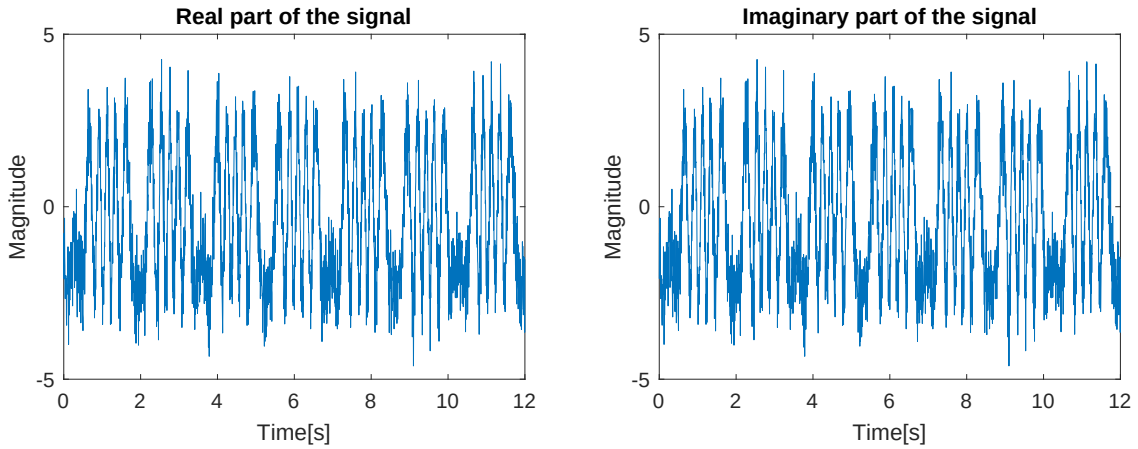

(a) Real (b) Imaginary

Figure 4.1: The real and imaginary parts of the signal ($SNR_{pulse} = 5$ dB, $\alpha_r = 5$ mm, $f_r = 0.3$ Hz)

Follow the instruction of EKF in (3.25), the simulation result is shown in Figure 4.2.

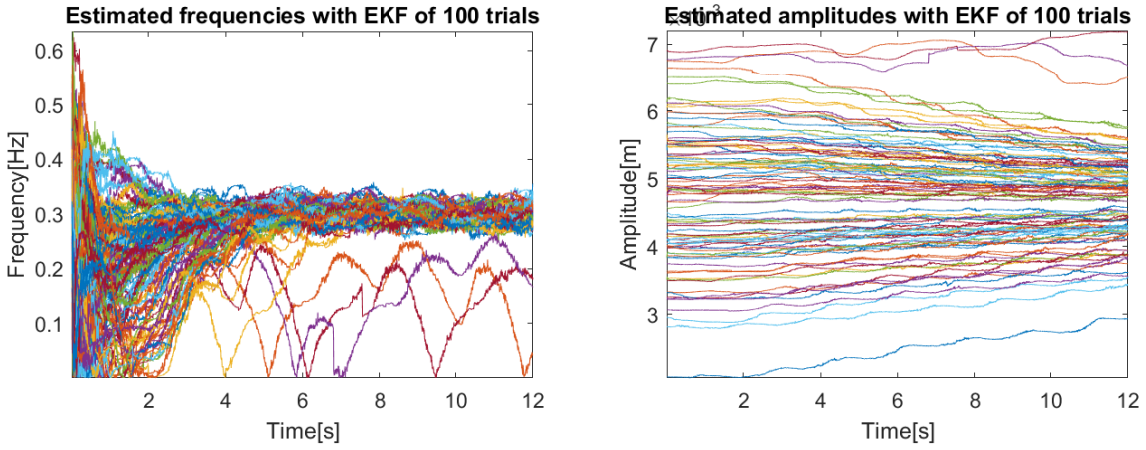

(a) Frequency (b) Amplitude

Figure 4.2: EKF estimators for frequency and amplitude of 100 trials($SNR_{pulse} = 5$ dB, $\alpha_r = 5$ mm, $f_r = 0.3$ Hz)

From the simulation results in Figure 4.2 with $SNR_{pulse} = 5$ dB and $\alpha_r = 5$ mm , $f_r = 0.3$ Hz for respiration model, it is shown that the estimators are unstable and not reliable. The reason for the this phenomenon is that the linearization for nonlinear model

is not sufficient enough since only the first order of its Taylor expansion is considered the nonlinearity is so strong that it violates the assumption of weekly nonlinearity for EKF. Random extra phase ϕ_e and initial phase φ_r are simulated for each trial in this result.

The simulation result for SNR_{pulse} increased from 5 dB to 20 dB, are shown in Figure 4.3.

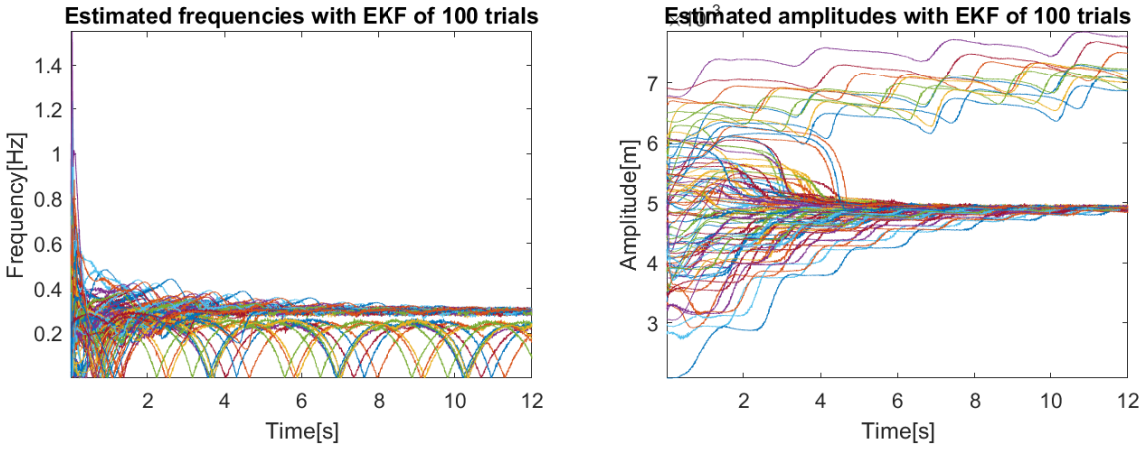

(a) Frequency (b) Amplitude

Figure 4.3: EKF estimators for frequency and amplitude of 100 trials($SNR_{pulse} = 20$ dB, $\alpha_r = 5$ mm, $f_r = 0.3$Hz)

From Figure 4.3, we observe that with higher $SNR_{pulse} = 20$ dB, noise is very week compared to the power of signal but the EKF estimator does not converge in some trials and its behavior in that trials is unstable. The reason of this unstable estimation is that there are sidelobes in the ambiguity function shown in Figure 2.8. With higher SNR_{pulse}, those sidelobes are more obvious for the EKF estimator which is very likely to converge around those sidelobes, if the initialization was not accurate enough. The estimator is initialized with random values for extra phase ϕ_e and initial phase φ_r. The initial values for magnitude h, amplitude α_r and frequency ω_r are selected from a normal distribution around their true values, respectively, $h_0 \sim \mathcal{N}(h_{ref}, (0.02 \cdot h_{ref})^2)$, $\alpha_{r,0} \sim \mathcal{N}(\alpha_r, (10^{-4})^2)$ and $\omega_{r,0} \sim \mathcal{N}(\omega_r, (0.1 \cdot 2\pi)^2)$.

In order to stable the EKF estimator, more observation samples are considered for one estimation instant. This is because the number of the observation samples k in each iteration contributes the process gain for each iteration, which helps to converge on the true mainlobe of the ambiguity function. Therefore, the total SNR for each iteration can be expressed as:

$$SNR_{total} = SNR_{pulse} + 10 \cdot \log_{10}(k+1). \tag{4.1}$$

Then, the observation model of this estimator in (3.9) becomes:

$$\begin{aligned}\mathbf{y}_t &= \mathbf{g}_m(\mathbf{x}_t) + \mathbf{u}_t \\ &= \begin{bmatrix} x_{4,t}\cos\left(Cx_{3,t}\sin(x_{1,t}+0\cdot T_s x_{2,t})+x_{5,t}\right) \\ \vdots \\ x_{4,t}\cos\left(Cx_{3,t}\sin(x_{1,t}+k\cdot T_s x_{2,t})+x_{5,t}\right) \\ x_{4,t}\sin\left(Cx_{3,t}\sin(x_{1,t}+0\cdot T_s x_{2,t})+x_{5,t}\right) \\ \vdots \\ x_{4,t}\sin\left(Cx_{3,t}\sin(x_{1,t}+k\cdot T_s x_{2,t})+x_{5,t}\right) \end{bmatrix} + \begin{bmatrix} \mathrm{Re}(u_t) \\ \vdots \\ \mathrm{Re}(u_t) \\ \mathrm{Im}(u_t) \\ \vdots \\ \mathrm{Im}(u_t) \end{bmatrix},\end{aligned} \tag{4.2}$$

where $k+1$ is the number of the observation samples in each iteration.

In order to minimize the problem of the EKF estimator converging around the side-lobes in Figure 2.8, the variance of frequency ω should be increased. The variance of the measured parameters are shown in Table 4.2.

Parameter	frequency, ω	amplitude, α	Magnitude, h	Extra phase, ϕ_e
Variance	100	9.00e-06	3	9.8696

Table 4.2: Variances of the measured parameters

The EKF estimator with $k = 100$ shows great capability of tracking the measured data as shown in Figure 4.4.

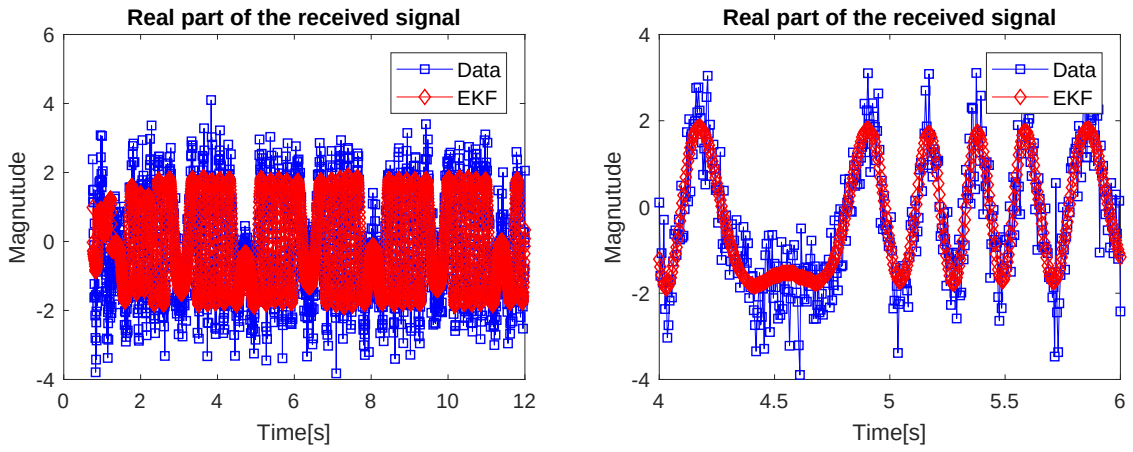

(a) Real part (b) Zoom in

Figure 4.4: Real part tracking ($SNR_{pulse} = 5$ dB, $\alpha_r = 5$ mm, $f_r = 0.3$ Hz, $k = 100$)

Performance analysis of that estimator is shown in Figure 4.5 and 4.6.

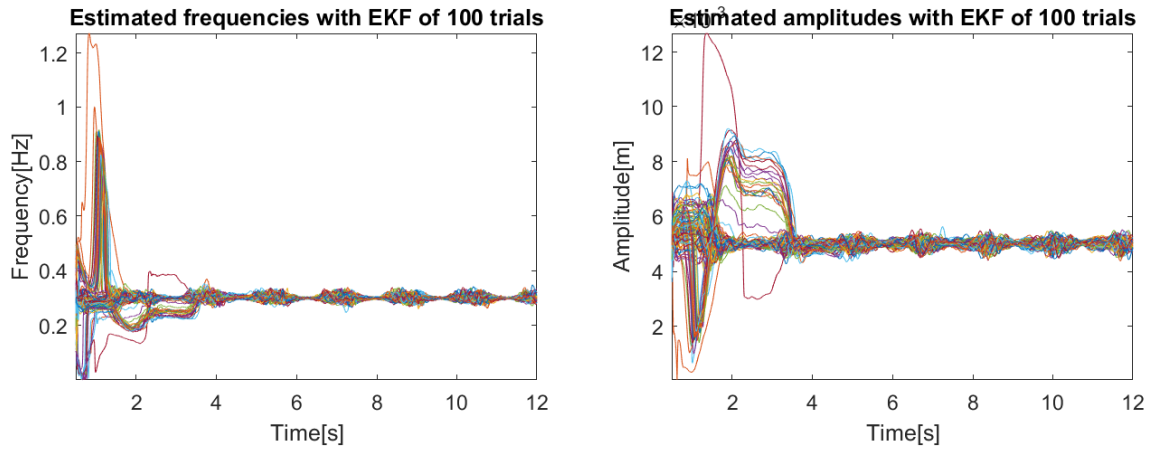

(a) Estimated frequencies of 100 trials (b) Estimated amplitudes of 100 trials

Figure 4.5: EKF estimators for frequency and amplitude of 100 trials($SNR_{pulse} = 5$ dB, $\alpha_r = 5$ mm, $f_r = 0.3$ Hz, $k = 100$)

Observed from Figure 4.5, the EKF estimators of both frequency and amplitude are converging on the true values at time around $t = 4s$.

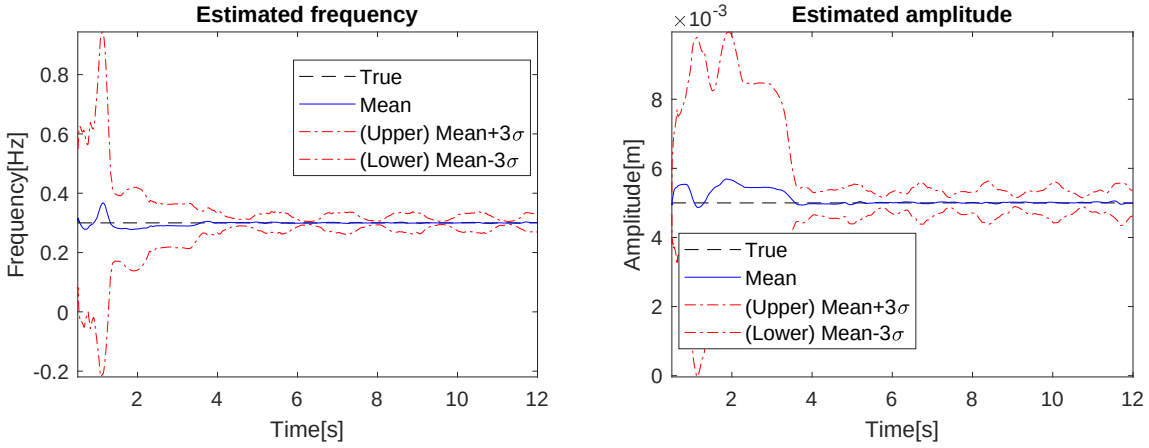

(a) Mean frequency and its variance (b) Mean amplitude and its variance

Figure 4.6: EKF estimators for frequency and amplitude of 100 trials($SNR_{pulse} = 5$ dB, $\alpha_r = 5$ mm, $f_r = 0.3$ Hz, $k = 100$)

Relatively big fluctuations are presented as 3σ line is 0.04 Hz away from the mean for frequency and 0.4 mm for amplitude shown in Figure 4.6. The fluctuations are caused by the big variance of frequency $\sigma_\omega = 100$.

For $k = 50$ and $k = 150$, the simulation result is shown in Figure 4.7.

It can be observed from Figure 4.7 that when the number of samples for each iteration k to be 50, the estimator diverges in some trials out of 100 trials thus is unstable. The

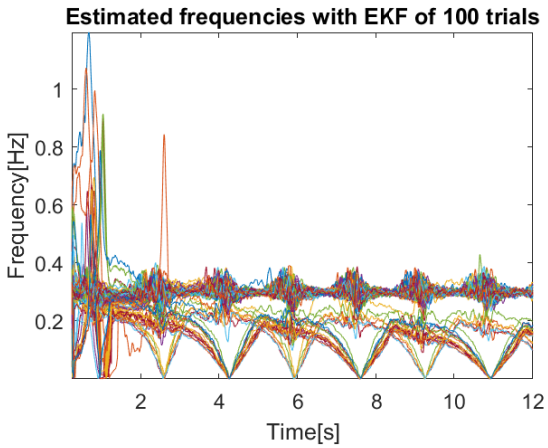

(a) Estimated frequencies of 100 trials, $k = 50$

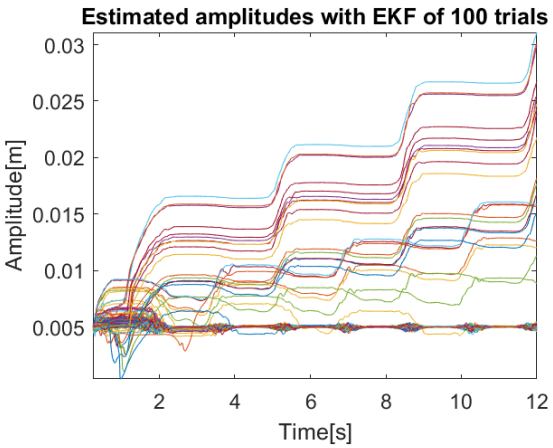

(b) Estimated amplitudes of 100 trials, $k = 50$

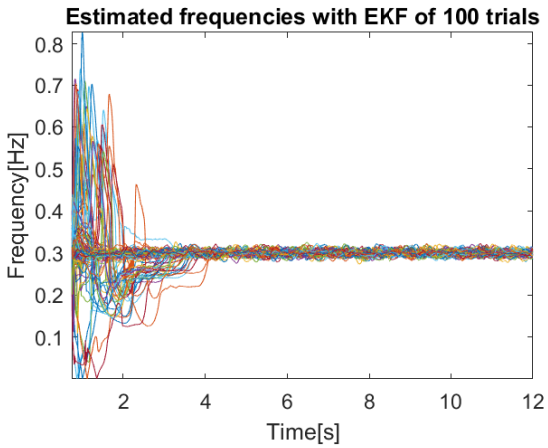

(c) Estimated frequencies of 100 trials, $k = 150$

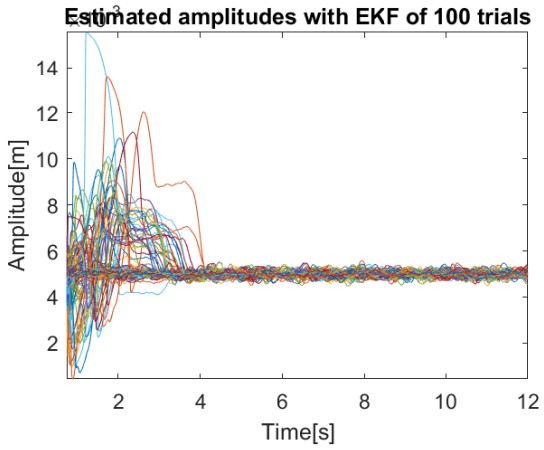

(d) Estimated amplitudes of 100 trials, $k = 150$

Figure 4.7: EKF estimator for frequency and amplitude with different values of k of 100 trials ($SNR_{pulse} = 5$ dB, $\alpha_r = 5$ mm, $f_r = 0.3$ Hz)

estimator with $k = 150$ is able to estimate the true value of both frequency and amplitude of respiration. Compared to the case when $k = 100$, the computational complexity and time increase and the estimator rely on more past measure data. Therefore, $k = 100$ is selected for this estimator.

If the value of the SNR for each pulse is $SNR_{pulse} = 0$ dB, the simulation results are shown in Figure 4.8.

Figure 4.8 shows that with the lower value of the SNR for each pulse $SNR_{pulse} = 0$ dB, the number of samples per iteration k should be increased to make the EKF estimator able to estimate the constant frequency and amplitude. The estimator with $k = 150$ converges at time around 7 s. The convergence time for this estimator with $SNR_{pulse} = 0$ dB is longer than that with $SNR_{pulse} = 5$ dB.

The simulation results for another set of parameters, $\alpha_r = 6$ mm, $f_r = 0.4$ Hz, are shown in Figure 4.9.

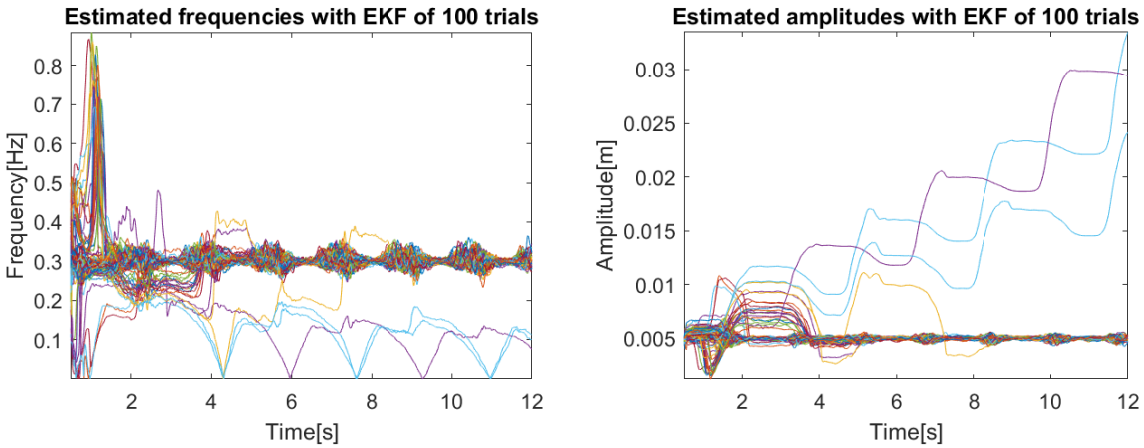

(a) Estimated frequencies of 100 trials, $k = 100$ (b) Estimated amplitudes of 100 trials, $k = 100$

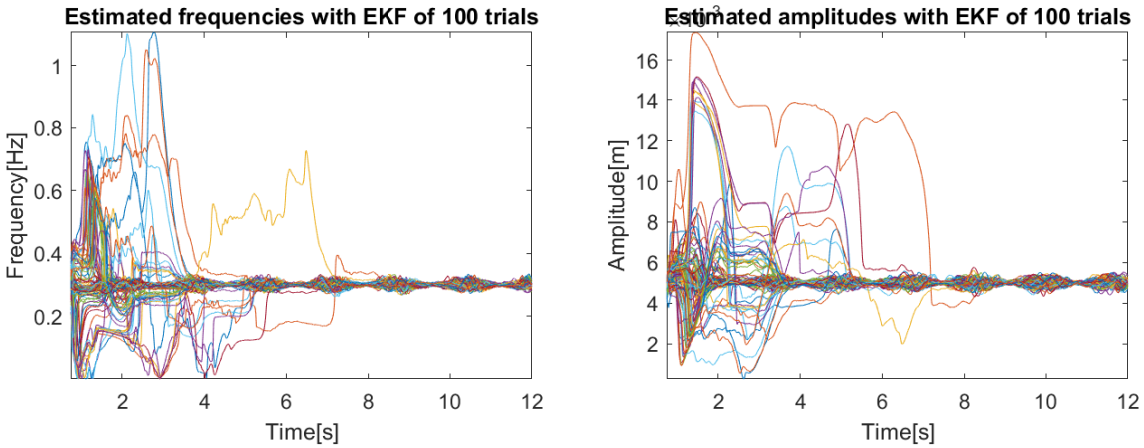

(c) Estimated frequencies of 100 trials, $k = 150$ (d) Estimated amplitudes of 100 trials,$k = 150$

Figure 4.8: EKF estimators for frequency and amplitude with different values of k of 100 trials ($SNR_{pulse} = 0$ dB, $\alpha_r = 5$ mm, $f_r = 0.3$ Hz)

Since the frequency and amplitude of the breathing is dynamic but not constant, the designed EKF estimator is tested by both dynamic frequency and amplitude. The dynamic model for frequency and amplitude of the respiration shown in Figure 4.10 is generated by a first-order autoregression model, which can be written as:

$$\begin{aligned} f_{dynamic} &= f_r + \Delta_{f,t} \\ \Delta_{f,t} &= q \cdot \Delta_{f,t-1} + \sqrt{1-q^2} \cdot \sigma_f, \end{aligned} \tag{4.3}$$

and,

$$\begin{aligned} \alpha_{dynamic} &= \alpha_r + \Delta_{\alpha,t} \\ \Delta_{\alpha,t} &= q \cdot \Delta_{\alpha,t-1} + \sqrt{1-q^2} \cdot \sigma_\alpha, \end{aligned} \tag{4.4}$$

where $q = 0.99999999$, $\sigma_f = 10$ and $\sigma_\alpha = 0.1$ in this simulation.

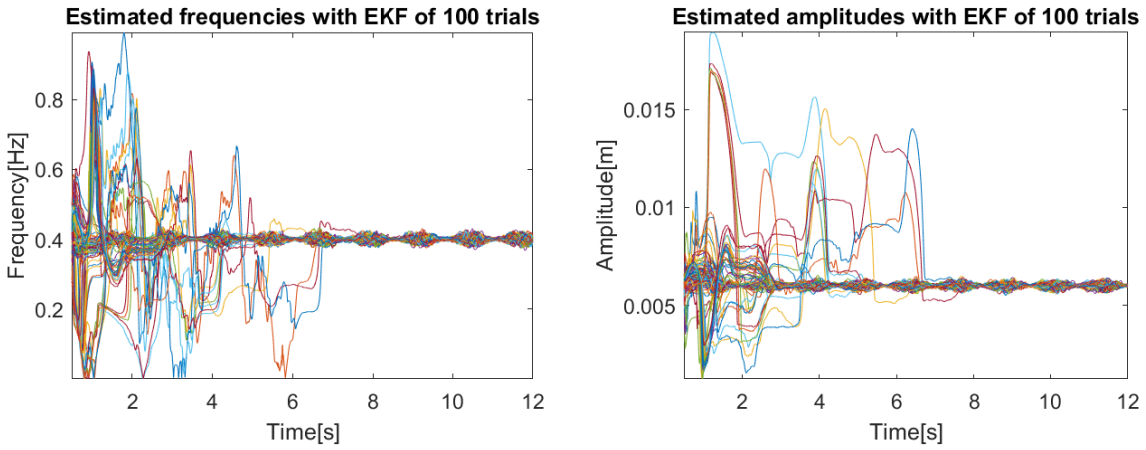

(a) Estimated frequencies of 100 trials (b) Estimated amplitude of 100 trials

Figure 4.9: EKF estimators for frequency and amplitude of 100 trials($SNR_{pulse} = 5$ dB, $\alpha_r = 6$ mm, $f_r = 0.4$ Hz, $k = 100$)

Both dynamic frequency and amplitude are assumed to change slowly within the typical values for respiration as listed in Table 2.1. The dynamic frequency and amplitude are reasonable if their change rate is small and their values are not exceeding their typical range.

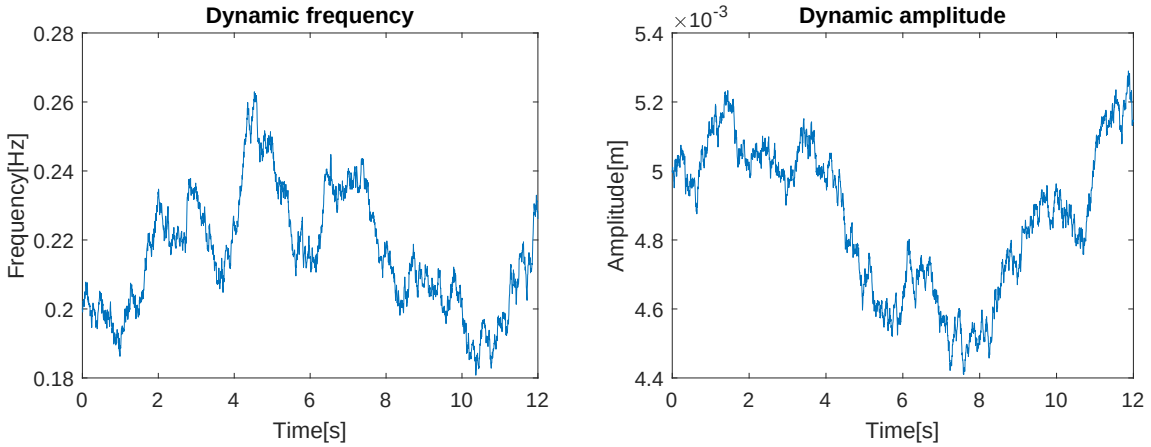

(a) Estimated frequencies of 100 trials (b) Estimated amplitude of 100 trials

Figure 4.10: Dynamic frequency and amplitude

Then, the performance of the EKF estimator to estimate dynamic respiration model is shown in Figure 4.11.

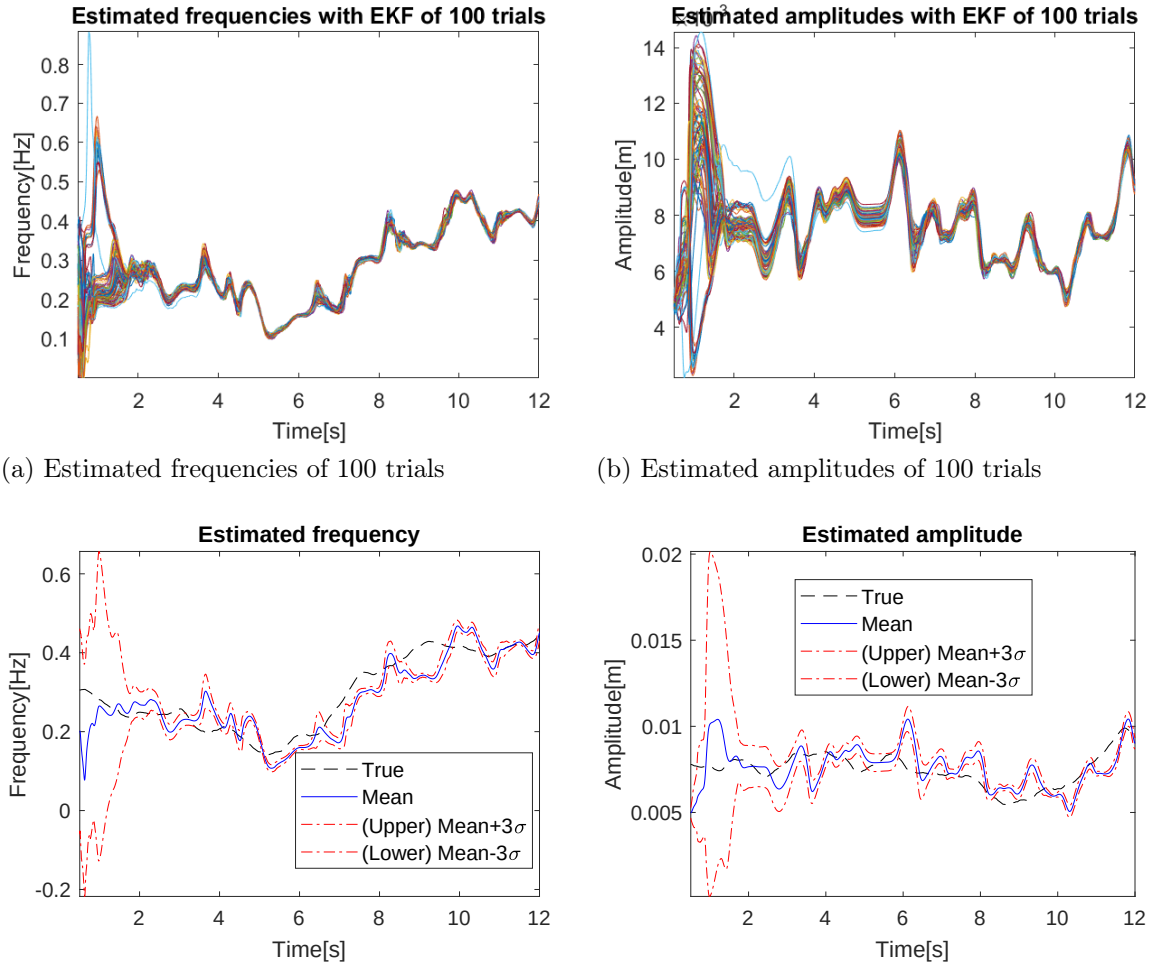

(a) Estimated frequencies of 100 trials

(b) Estimated amplitudes of 100 trials

(c) Mean frequency and its variance

(d) Mean amplitude and its variance

Figure 4.11: EKF estimator for dynamic frequency and amplitude of 100 trials ($SNR_{pulse} = 5$ dB, $k = 100$)

It is shown in Figure 4.11 that the estimator is able to track dynamic parameters of respiration. The fluctuation around the estimated mean value is due the fact that both frequency and amplitude are continuously changing over time and estimated frequency and amplitude are the average values over the sliding observation window.

4.1.2. Extended Kalman Filter Based On Phase History

Assuming the signal with high SNR for each pulse and the noise in phase is Gaussian, then EKF estimator can be applied to the phase history with only four parameters: frequency, amplitude, initial phase and extra average phase θ_{av}. The measured data is expressed as in (3.20). Then, the NCF model for this EKF estimator is expressed in (3.16)-(3.22).

In order to avoid the problem of the EKF estimator converging around the sidelobes in Figure 2.8, the variance of frequency ω should be increased. The variance of the measured parameters are shown in Table 4.3.

Parameter	frequency, ω	amplitude, α	average phase θ_{av}
Variance	10.97	2.78e-05	0.0278

Table 4.3: Variances of the measured parameters

Follow the instruction of EKF in (3.25), the simulation results are shown in Figure 4.12.

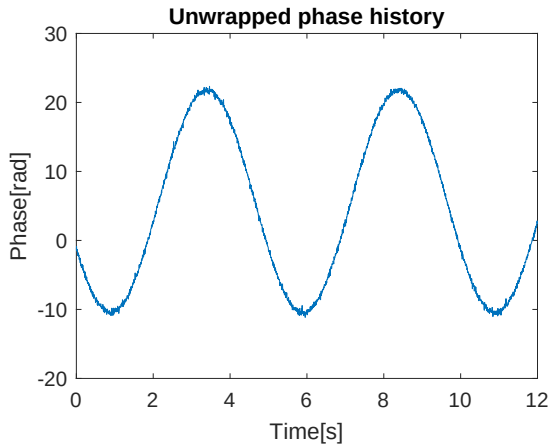

(a) Unwrapped phase history

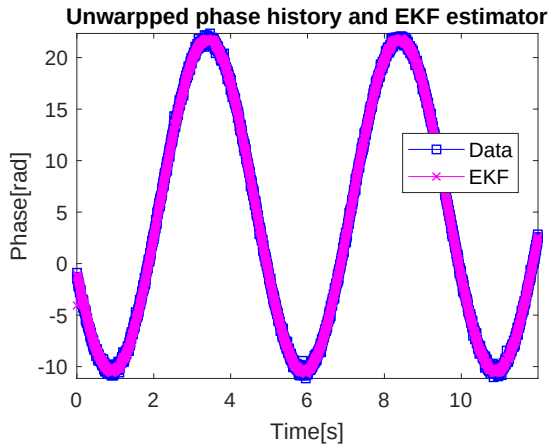

(b) Phase history tracking

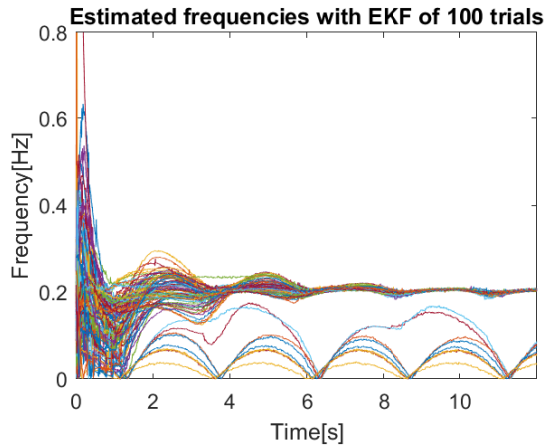

(c) Estimated frequencies of 100 trials

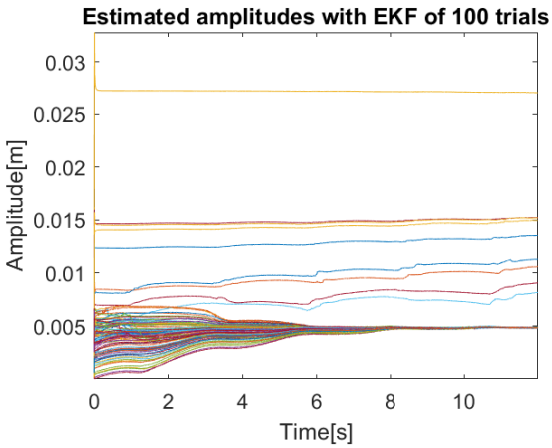

(d) Estimated amplitudes of 100 trials

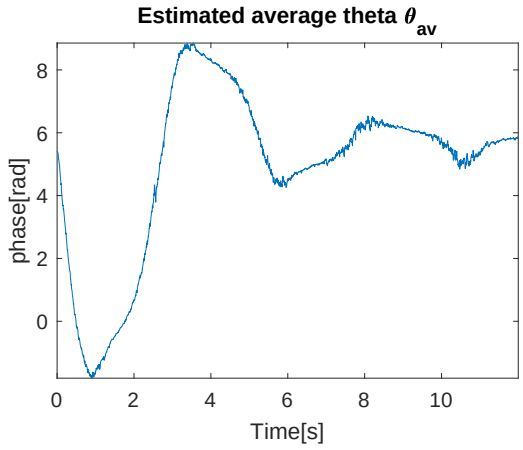

(e) Estimated average phase θ_{av}

Figure 4.12: EKF estimator for frequency and amplitude based on phase history of 100 trials($SNR_{pulse} = 10$ dB, $\alpha_r = 5$ mm, $f_r = 0.2$ Hz)

From Figure 4.12, observation can be made that this EKF estimator based on phase history can track the phase history but the estimated frequency and amplitude do not

always converge on their true values, respectively. Therefore, the estimator is not reliable all the times. This is because the average phase θ_{av} takes part of the role of frequency and amplitude for the phase history evolution as shown in Figure 4.12e. Anther reason for this divergence is that with the existence of the average phase θ_{av}, the estimator sometimes attempts to estimator the zero frequency part which appears in the power spectrum for this sinusoidal wave with DC component.

The estimator is initialized with random values for average phase θ_{av} and initial phase φ. The initial values for amplitude α_r and frequency ω_r are selected from a normal distribution around their true values, respectively, $\alpha_{r,0} \sim \mathcal{N}(\alpha_r, (10^{-3})^2)$ and $\omega_{r,0} \sim \mathcal{N}(\omega_r, (0.5 \cdot 2\pi)^2)$.

Larger number of observation samples for each estimation are considered to stable the estimator. Then, observation model becomes:

$$\begin{aligned}\mathbf{y}_t &= \mathbf{g}_m(\mathbf{x}_t) + \mathbf{u}_t \\ &= \begin{bmatrix} Cx_{3,t}\sin(x_{1,t} + +0 \cdot T_s x_{2,t}) + x_{4,t} \\ \vdots \\ Cx_{3,t}\sin(x_{1,t} + +k \cdot T_s x_{2,t}) + x_{4,t} \end{bmatrix} + \begin{bmatrix} u_t \\ \vdots \\ u_t \end{bmatrix},\end{aligned} \tag{4.5}$$

where $k+1$ is the number of the observation samples in each iteration and the covariance matrix of the measurement noise is:

$$\begin{aligned}\mathbf{R} &= \mathbb{E}\left\{\mathbf{u}_t \mathbf{u}_t^T\right\} \\ &= \begin{bmatrix} \sigma_u^2 & & \\ & \ddots & \\ & & \sigma_u^2 \end{bmatrix}.\end{aligned} \tag{4.6}$$

Then, with $k = 100$, the performance of this EKF estimator is shown in Figure 4.13.

Observation can be made from Figure 4.13 that the EKF estimator with larger observation samples for each estimation update converges on around the true values of frequency and amplitude at time about 6 s. And the estimated average phase θ_{av} becomes stable as compared to the case when $k = 0$. The choice of $k = 100$ is well selected based on the trade-off between the performance of the estimator and computational complexity and time. Decreasing the value of k will lead to unstable estimator and increasing k does not give a better performance but increasing the computational complexity and time.

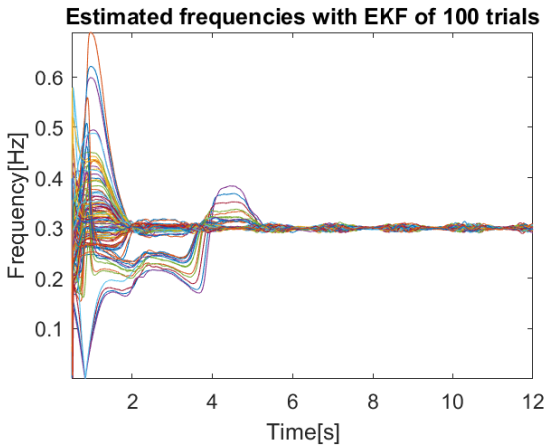

(a) Estimated frequencies of 100 trials

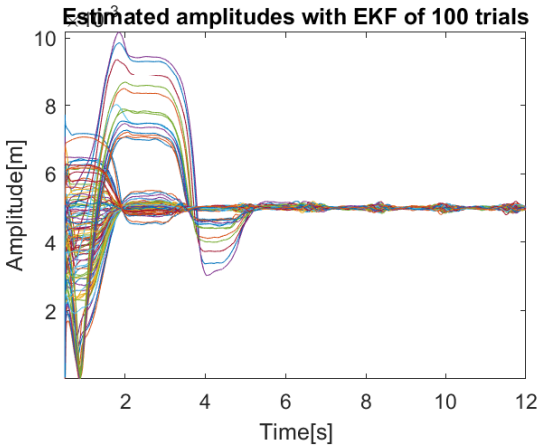

(b) Estimated amplitudes of 100 trials

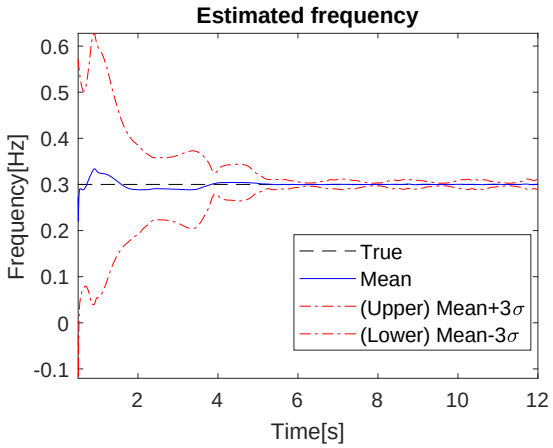

(c) Mean frequency and its variance

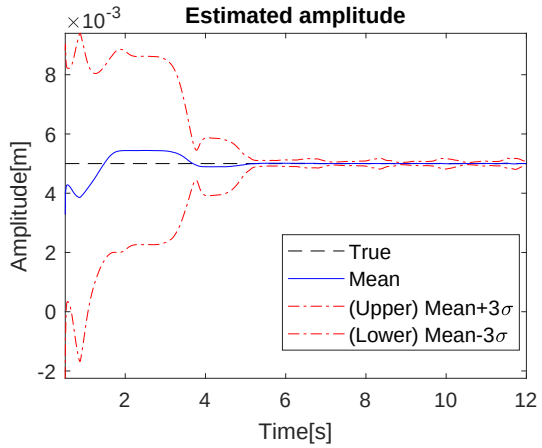

(d) Mean amplitude and its variance

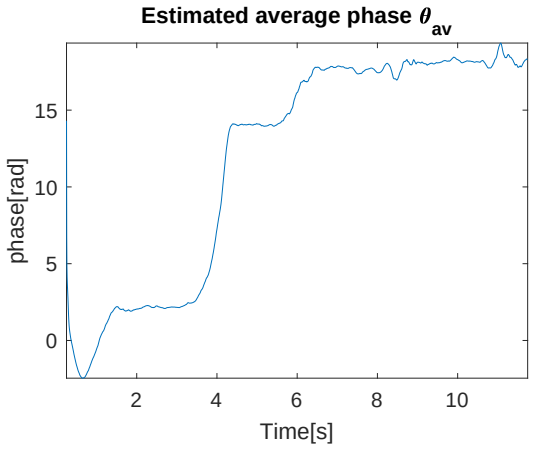

(e) Estimated average phase θ_{av}

Figure 4.13: EKF estimator for frequency and amplitude based on phase history of 100 trials($SNR_{pulse} = 10$ dB, $k = 100$, $\alpha_r = 5$ mm, $f_r = 0.3$ Hz)

For $k = 50$ and $k = 150$, the simulation result is shown in Figure 4.14.

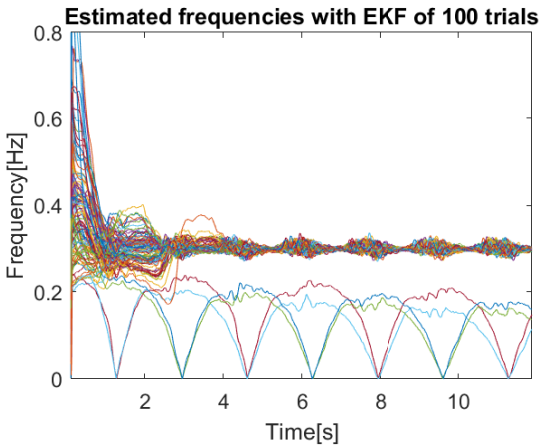

(a) Estimated frequencies of 100 trials, $k = 50$

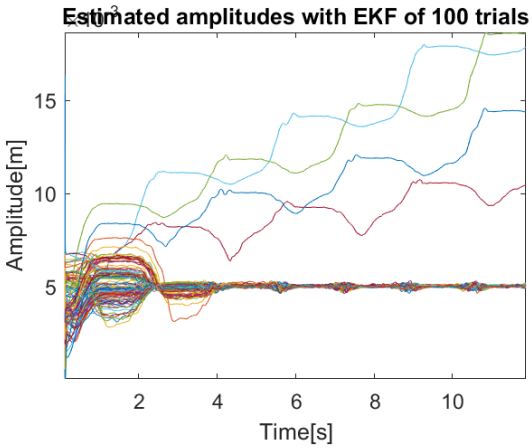

(b) Estimated amplitudes of 100 trials, $k = 50$

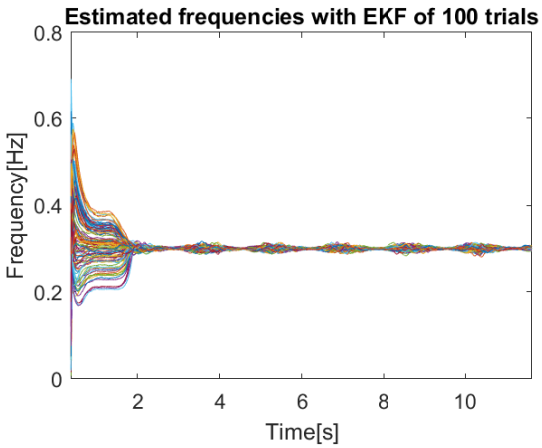

(c) Estimated frequencies of 100 trials, $k = 150$

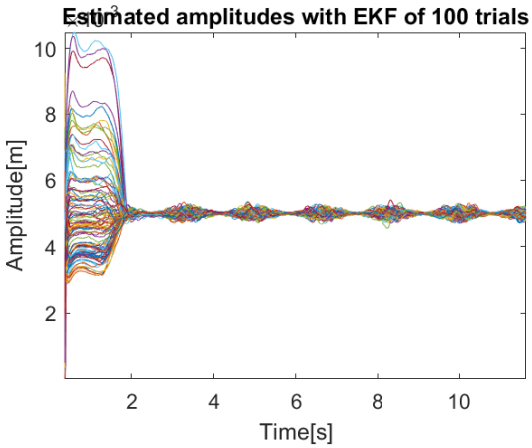

(d) Estimated amplitudes of 100 trials, $k = 150$

Figure 4.14: EKF estimator for frequency and amplitude based on phase history with different values of k of 100 trials ($SNR_{pulse} = 10$ dB, $\alpha_r = 5$ mm, $f_r = 0.3$ Hz)

From Figure 4.14, it is shown that when $k = 50$, the estimator is not stable and diverges for some trials while the estimator with $k = 150$ converges faster than the case when $k = 100$. However, the computational complexity and time increases with larger value of k. Therefore, the reasonable value of $k = 100$ is selected which makes the estimator stable without relying too much on the past data.

For a different set of frequency $f_r = 0.2$ Hz and amplitude $\alpha_r = 8$ mm of respiration, the simulation with $k = 100$ result is shown in Figure 4.15.

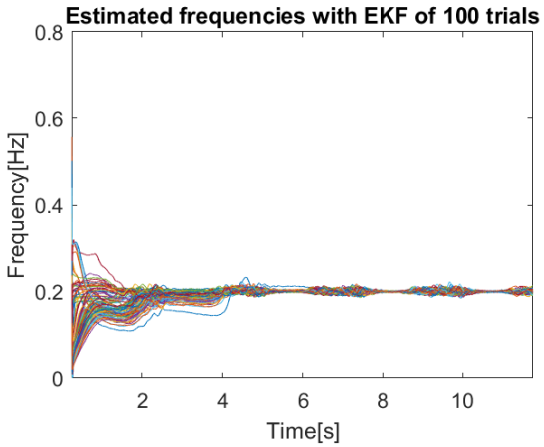

(a) Estimated frequencies of 100 trials

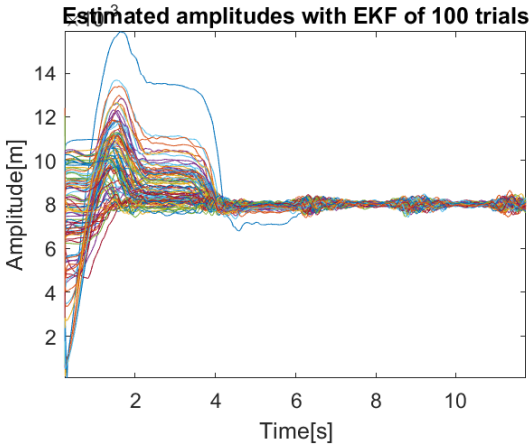

(b) Estimated amplitudes of 100 trials

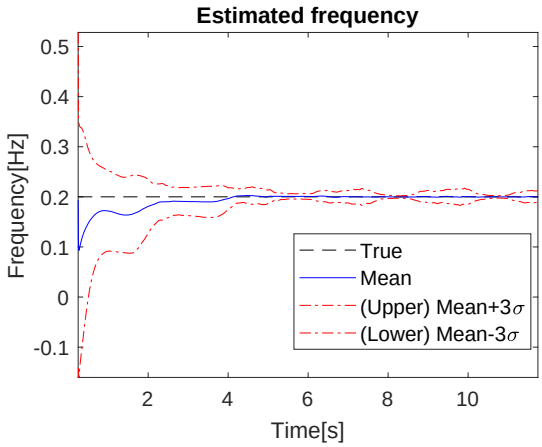

(c) Mean frequency and its variance

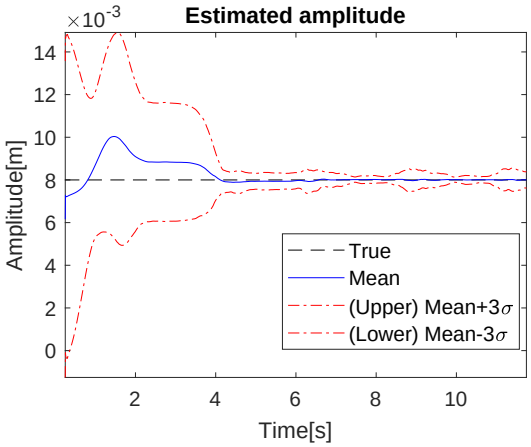

(d) Mean amplitude and its variance

Figure 4.15: EKF estimator for frequency and amplitude based on phase history of 100 trials ($SNR_{pulse} = 10$ dB, $k = 100$, $\alpha_r = 8$ mm, $f_r = 0.2$ Hz)

This EKF estimator is reliable for different values of the frequency and amplitude of respiration as observed from Figure 4.15.

If the SNR for each transmitted pulse is lower, $SNR_{pulse} = 6$ dB, then the simulation result is shown in Figure 4.16.

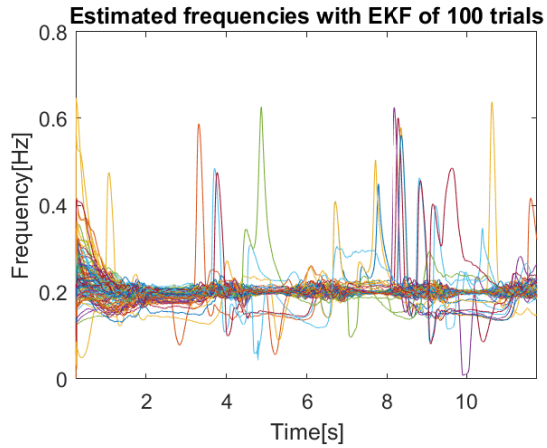

(a) Estimated frequencies of 100 trials

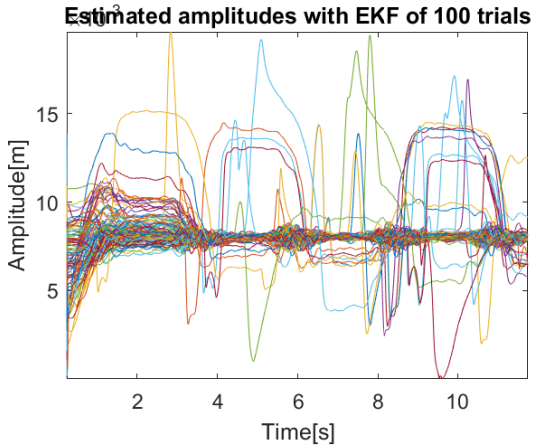

(b) Estimated amplitudes of 100 trials

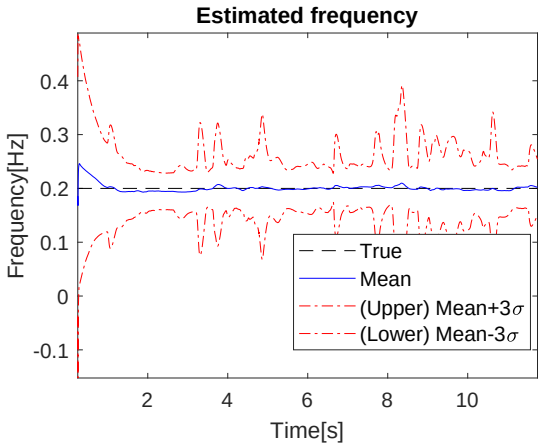

(c) Mean frequency and its variance

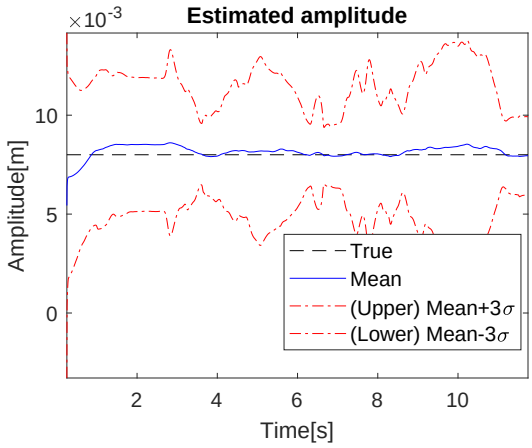

(d) Mean amplitude and its variance

Figure 4.16: EKF estimator for frequency and amplitude based on phase history of 100 trials ($SNR_{pulse} = 6$ dB, $k = 100$, $\alpha_r = 8$ mm, $f_r = 0.2$ Hz)

With lower SNR for each transmitted pulse, $SNR_{pulse} = 6$ dB, this estimator is fluctuating over the observation time and the variances of both frequency and amplitude become larger as compared to the case when $SNR_{pulse} = 10$ dB. This is because the phase noise can not be assumed to be Gaussian and the average phase θ_{av} is no longer nearly constant over the time as shown in Figure 3.2b due to the unwrapped process with larger phase noise.

Although the problem for this estimator when $SNR_{pulse} = 6$ dB, the variances of the estimated frequencies and amplitudes of 100 trials for the same SNR, $SNR_{pulse} = 6$ dB, can be decreased by increasing the number of the observation samples in each iteration k is increased to be $k = 199$ and the corresponding simulation result is shown in Figure 4.17.

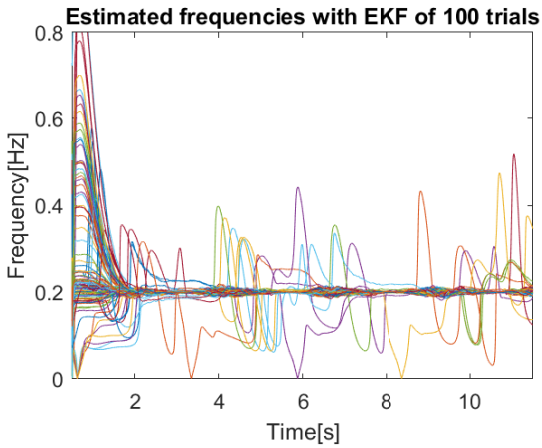

(a) Estimated frequencies of 100 trials

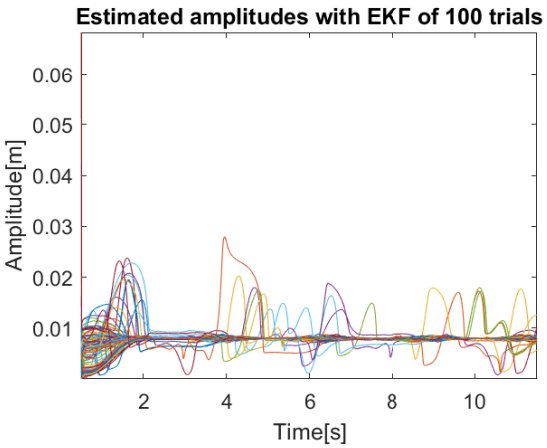

(b) Estimated amplitudes of 100 trials

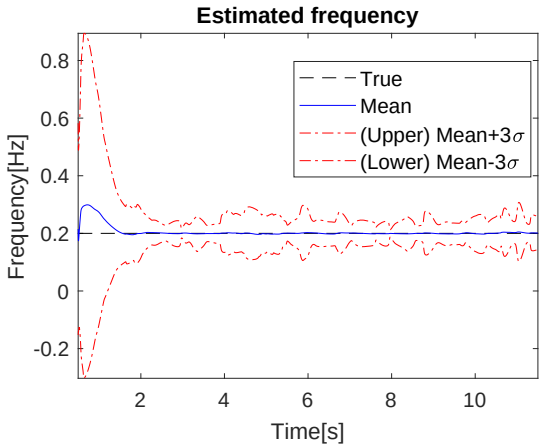

(c) Mean frequency and its variance

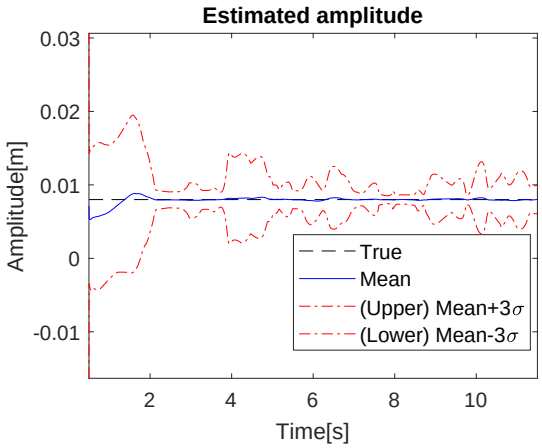

(d) Mean amplitude and its variance

Figure 4.17: EKF estimator for frequency and amplitude based on phase history of 100 trials ($SNR_{pulse} = 6$ dB, $k = 199$, $\alpha_r = 8$ mm, $f_r = 0.2$ Hz)

From Figure 4.17, we can observe that the variances of the estimated frequencies and amplitudes of 100 trials are reduced by increasing the number of the observation samples in each iteration $k = 199$ as compared to the case when $k = 100$ with the same $SNR_{pulse} = 6$ dB. The price for this reduce variances are the increased computational complexity and time for each iteration. In addition, the problem occurring in process of unwrapping can not be solved by increasing the number of the observation samples in each iteration.

Then, the performance of this EKF estimator with $SNR_{pulse} = 10$ dB and $k = 100$ is shown in Figure 4.18.

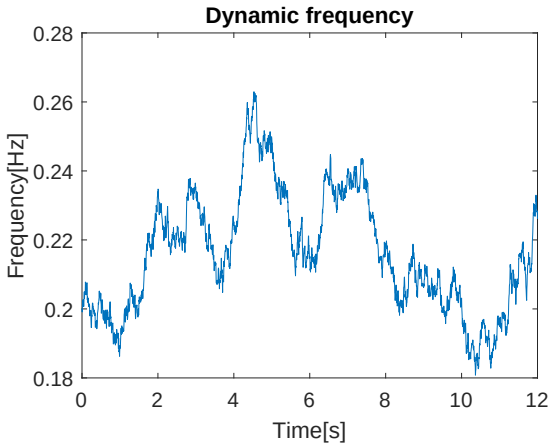

(a) Dynamic frequency

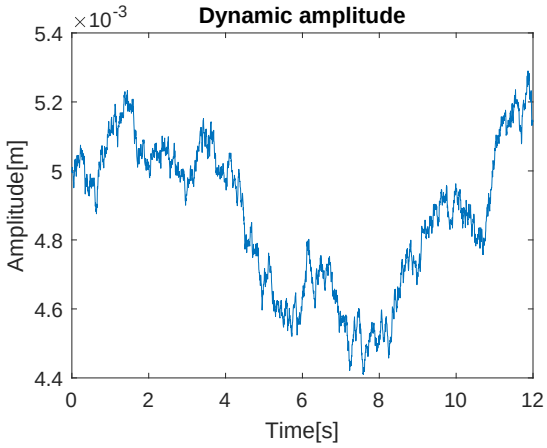

(b) Dynamic amplitude

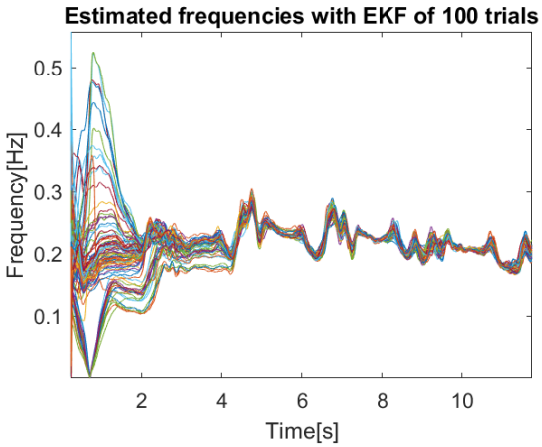

(c) Estimated frequencies of 100 trials

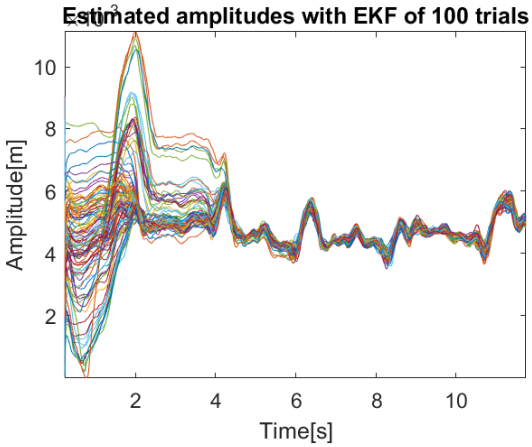

(d) Estimated amplitudes of 100 trials

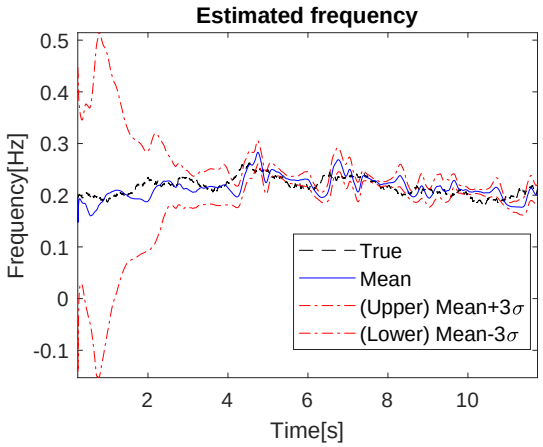

(e) Mean frequency and its variance

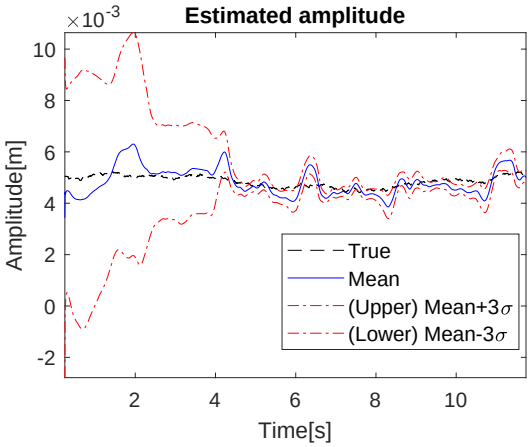

(f) Mean amplitude and its variance

Figure 4.18: EKF estimator for dynamic frequency and amplitude based on phase history of 100 trials($SNR_{pulse} = 10$ dB, $k = 100$)

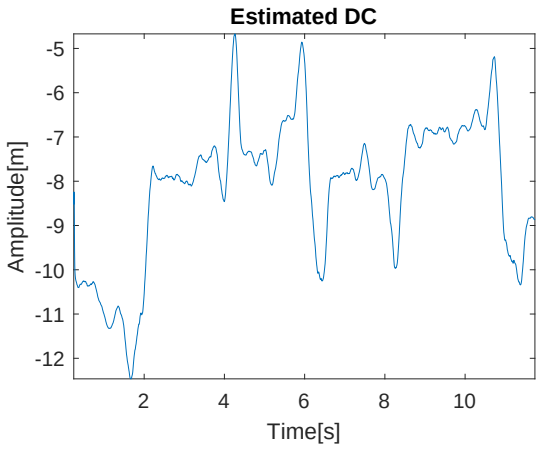

htb!

Figure 4.19: Estimated average phase θ_{av}

As we can observe from Figure 4.18, this EKF estimator is stable and converging around the true values of both frequency and amplitude of respiration. The average time for convergence of this estimator is about 4s. The fluctuation of this estimator around the true is caused by the fluctuation of the estimated average phase θ_{av}. When the amplitude and/or the frequency is changed over time, average phase θ_{av} is considered to be changed by this estimator as well rather than being thought to be stable all the time as shown in Figure 4.19.

In addition, there is a delay between the estimated frequency and amplitude and their true values at each time instant due to the longer observation window for each estimation.

4.1.3. Particle filter

As mentioned above, KF performs the same as PF in linear Gaussian case. In nonlinear and/or non-Gaussian case, PF is considered to have good performance.

Assumed that the magnitude h and the extra phase ϕ_e of the measured signal in (2.22) are known, the observation model can be expressed in (4.7) and SIS estimation is performed in follows.

$$y(n) = \exp\left(j\frac{4\pi f_c}{c}\left(\alpha_r \cdot \sin(2\pi f_r \cdot n + \varphi_r)\right)\right) + u, \tag{4.7}$$

where u is the complex Gaussian noise.

For a set of particles of $N = 100 \times 100 \times 100$ ($amplitude \times frequency \times initialphase$ and $a_r \sim \mathcal{U}(3e-3, 8e-3)$ m, $f_r \sim \mathcal{U}(0.1, 0.8)$ Hz and $\varphi_r \sim \mathcal{U}(0, 2\pi)$ rad), *i.e.*, the particle can be expressed as:

$$y^i(k) = \exp\left(j \cdot \frac{4\pi f_c}{c} \cdot a_r^i \cdot \sin(2\pi f_r^i \cdot k \cdot PRI + \varphi_r^i)\right). \tag{4.8}$$

Their associated importance weights can be computed based on the idea of MMSE:

$$\omega_k^i = \frac{1}{|y^i(k) - y(k)|^2}, \tag{4.9}$$

or based on maximum likelihood (ML):

$$\omega_k^i = \frac{1}{\sqrt{\pi\sigma_u^2}} \exp\left(\frac{|y^i(k) - y(k)|^2}{\sigma_u^2}\right). \tag{4.10}$$

During the process of SIS, the associated importance weights are preserved and updated by multiplying the newly obtained importance weights. Then, the three parameters are computed by taking the mean according to the normalized weights:

$$\hat{a}_{r,k} = \sum_{i=1}^{N} \omega_k^i a_r^i,$$
$$\hat{f}_{r,k} = \sum_{i=1}^{N} \omega_k^i f_r^i,$$
$$\hat{\varphi}_{r,k} = \sum_{i=1}^{N} \omega_k^i \varphi_r^i.$$

The simulation result is shown in Figure 4.20.

It is observed from Figure 4.20 that convergences have achieved for all three parameters with both MMSE and ML importance weights samplings at around $2.5s$. The

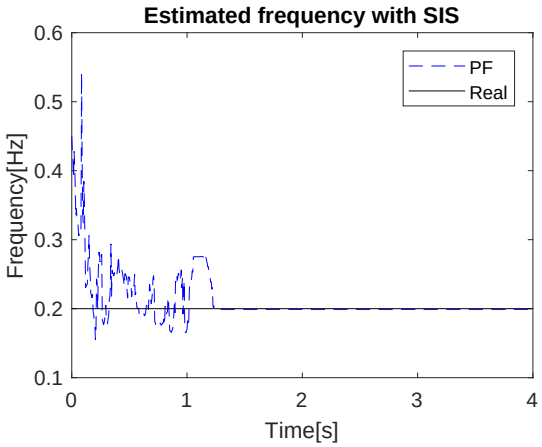

(a) Frequency, MMSE

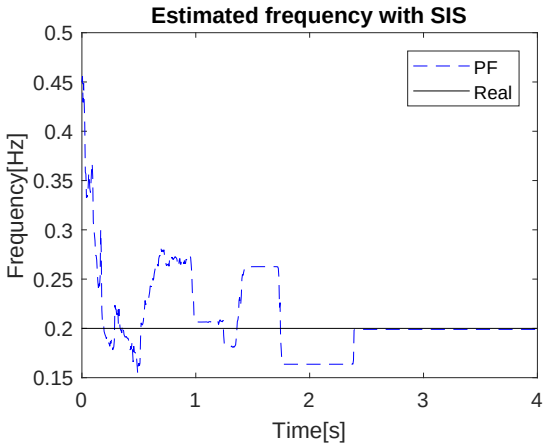

(b) Frequency, ML

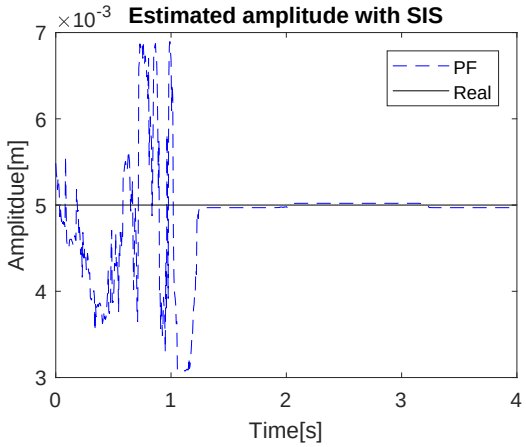

(c) Amplitude, MMSE

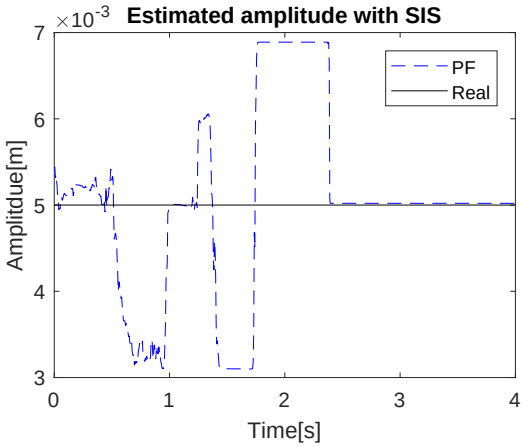

(d) Amplitude, ML

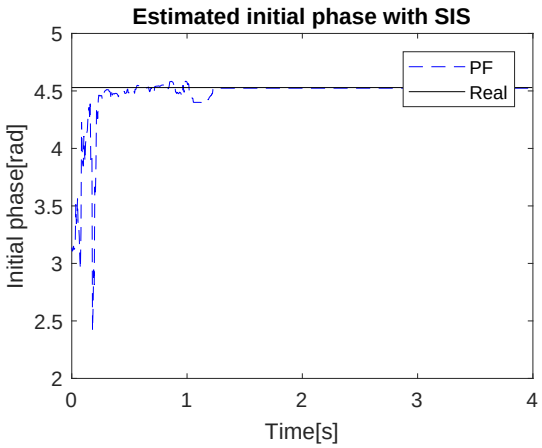

(e) Initial phase, MMSE

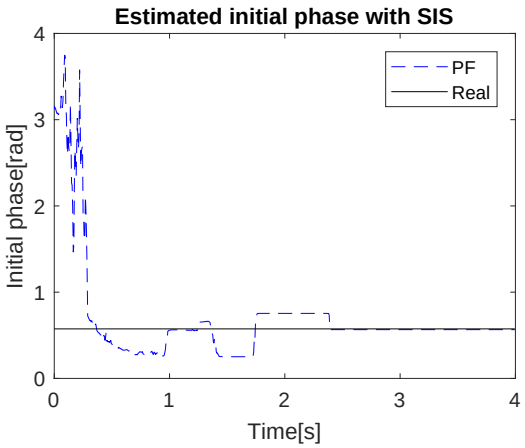

(f) Initial phase, ML

Figure 4.20: SIS estimators with different importance weights samplings: MMSE and ML ($SNR_{pulse} = 8dB$, $\alpha_r = 5mm$, $f_r = 0.2Hz$ and random initial phase)

possible reason why these estimators converge at this time instance of $2.5s$ is that there are many harmonics for this sinusoidal wave in phase thus there are many possible combinations of frequencies and amplitudes can display the same phase changing within half of the measured breathing period which is exactly the time instant $2.5s$.

The simulation times for these two algorithms, MMSE and ML, are about $41.6s$ and $46.2s$ with the same number of particles of 10^6. These times are much larger than the observation time of $4s$. Therefore, if the magnitude h and the extra phase ϕ_e of the measured signal are unknown, enormous number of particles are required and the computational time is increased correspondingly.

Initialization:

Since the computational time is strongly proportional to the number of particles, estimating some unknown but constant parameters in the initial stage is considered, such as the magnitude h and the extra phase ϕ_e of the measured signal and the initial phase φ_r of the breathing motion.

Take the phase history expressed in (3.14) as the measured data, the magnitude h and the extra phase ϕ_e of the measured signal is no longer necessary for estimation while the average phase θ_{av} needs to be estimated. Since the minimal frequency of respiration is $f_{r,min} = 0.1Hz$. Therefore, in order to obtain the correct values of φ_r and θ_{av}, the required time T_{ini} for initialization is:

$$T_{ini} = 0.75 \times \frac{1}{f_{r,min}} = 7.5[s]$$

Dynamic tracking:

As mentioned in the previous chapter, there is a major drawback for SIS algorithm. As process goes, the value of the importance weight of the desired particle gradually approaches the value of 1, resulting in forcing that values of other particles almost to be zeros. Consequently, only the importance weight of the desired particle contributes the final estimator while other particles losing their influences. Dynamic of this SIS estimator is lost and this property performs well only for constant parameters.

In order to have the ability to track dynamic breathing activity, SIR with bootstrap algorithm is going to be used. However, resampling process, including searching and copying particles with higher importance weights, requires much more time than just multiplying importance weights in each iteration in SIS. In addition, resampling does not guarantee to avoid the problem of weight degeneracy [37].

Therefore, some modification can be applied into the algorithm of SIS. Referred to (3.28), an annealing factor α_w is added to the importance weights before it is propagated

to the newly obtained one:

$$\mathbf{w}_t^{(i)} = (\mathbf{w}_{t-1}^{(i)})^{\alpha_w} \times \frac{p(\mathbf{y}_t|\mathbf{x}_t^{(i)})p(\mathbf{x}_t^{(i)}|\mathbf{x}_{t-1}^{(i)})}{\pi(\mathbf{x}_t^{(i)}|\mathbf{x}_{0:t-1}^{(i)}, \mathbf{y}_{1:t})},$$

where $0 < \alpha_w < 1$, reducing the influence of previous importance weights [37].

With the annealing factor $\alpha_w = 0.986$ and the set of particles of $N = 200 \times 200$ ($amplitude \times frequency$, the modified estimation for dynamic frequency and amplitude is shown in Figure 4.21. The reduced number of particles is based on the good estimation of the initial phase φ_r and the average phase θ_{av}. The value of the annealing factor $\alpha_w = 0.986$ is selected to alleviate the degeneracy problem so that the estimator is able to track the dynamic parameters. Smaller α_w lead to slow convergence and larger one cannot alleviate the degeneracy problem.

From Figure 4.21, it is shown that this modified sequential PF estimator is able to track dynamic parameters. The three sigma lines in both Figure 4.21a and Figure 4.21b converges at time $t = 9$ s, diverges from $t = 9$ s to $t = 13$ s and is going to converge again. This corresponds to the behavior of dynamic frequency. When frequency stays constant, the estimator converges quickly, within 2 s in this case. And the estimator diverges when frequency is changing.

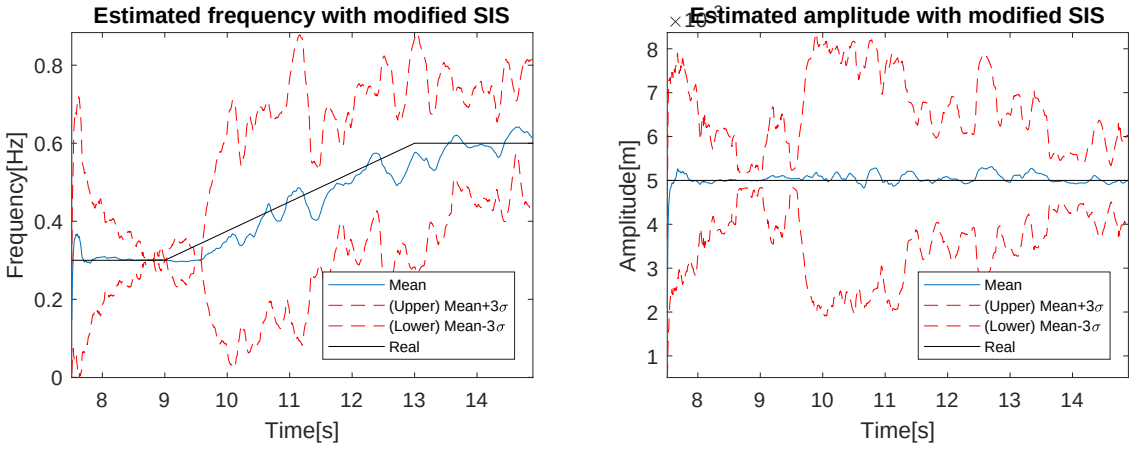

(a) Estimated frequency (b) Estimated Amplitude

Figure 4.21: Frequency and amplitude estimators with modified SIS algorithm over 100 trials (MMSE), $SNR_{pulse} = 8$ dB

The computation time for each new data is only 0.007 s, very close to the sampling time $PRI = 0.005$ s. Therefore, fast online tracking is available.

4.2. Estimation for Respiration with Existence of Heartbeat

In this section, estimation for frequency and amplitude of respiration is performed with the existence of heartbeat, which is corresponding to the case in reality.

From Table 2.1, the frequency $f_h = 1.35$ Hz and amplitude $\alpha_h = 0.5$ mm of heartbeat are selected. With dynamic respiratory frequency and amplitude shown in Figure 4.18a and 4.18b and sin for heartbeat considered, movement of the chest is shown in Figure 4.22.

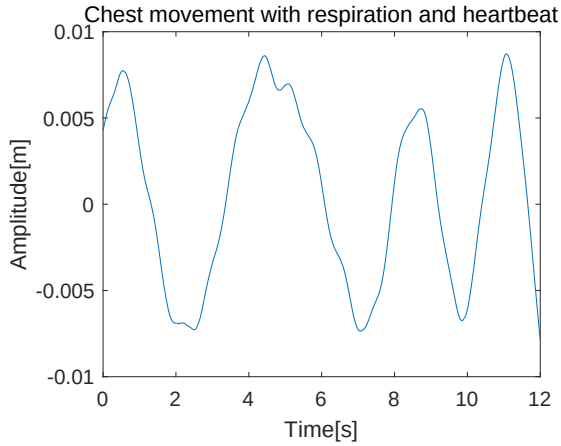

Figure 4.22: Chest movement with respiration and heartbeat (Dynamic f_r and α_r, $f_h = 1.35$ Hz and $\alpha_h = 0.5$ mm)

With the EKF estimator for respiration based I/Q demodulation, the simulation result, with $SNR_{pulse} = 5$ dB and the number of samples for each pulse $k + 1 = 101$, is shown in Figure 4.23.

It can be observed from Figure 4.23 that the estimator cannot track the real part of the signal properly and the estimated frequency and amplitude for respiration diverged, resulting in the deviations of their estimated mean of 100 trials, respectively, thus large variances. This is because the additive movement of chest caused by heartbeat can lead the estimator to converge around the sidelobes of the ambiguity function. Another reason for this divergence is that the chest movement caused by heartbeat is absent from both of the state model and observation model which cannot be treated as noise perturbation.

With the EKF estimator for respiration based on phase history, the simulation result, with $SNR_{pulse} = 10$ dB and the number of samples for each pulse $k + 1 = 101$, is shown in Figure 4.24.

It is shown in Figure 4.24 that the estimator performs track the phase history and shows convergence for both frequency and amplitude around their true values for res-

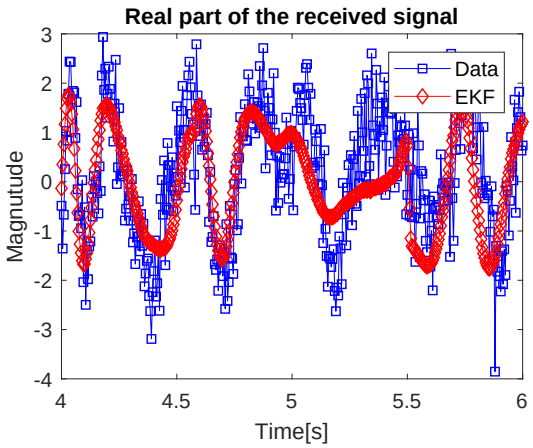

(a) Real part tracking

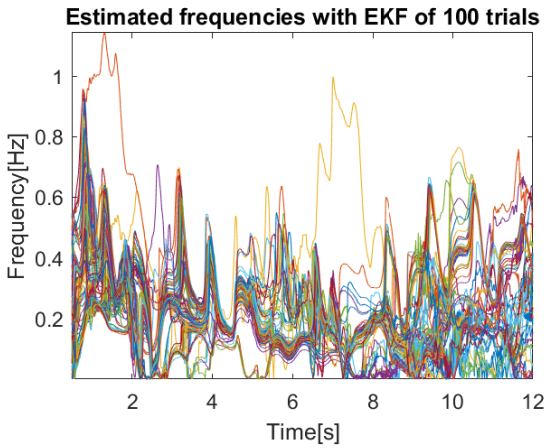

(b) Estimated frequencies of 100 trials

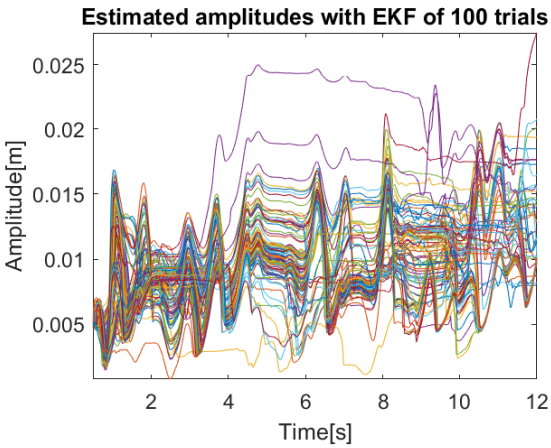

(c) Estimated amplitudes of 100 trials

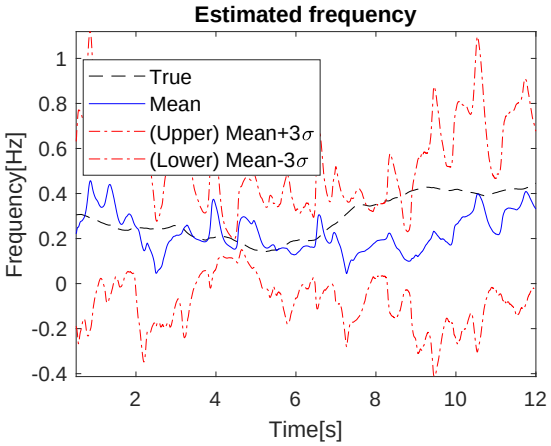

(d) Mean frequency and its variance

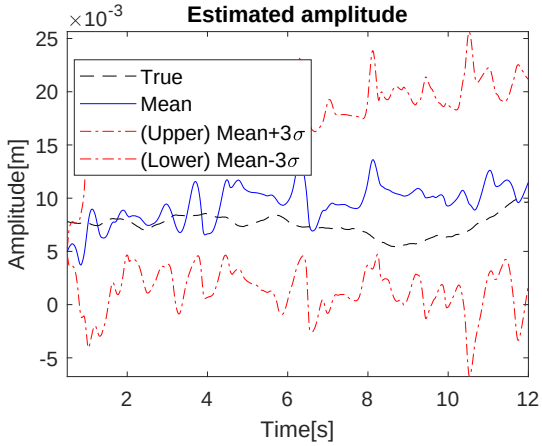

(e) Mean amplitude and its variance

Figure 4.23: EKF estimator for dynamic respiratory frequency and amplitude based on I/Q demodulation of 100 trials (Dynamic f_r and α_r, $f_h = 1.35$ Hz and $\alpha_h = 0.5$ mm, $SNR_{pulse} = 5$ dB)

piration. The estimated frequency and amplitude fluctuates around their true values every 0.74 s which exactly corresponds to the period of heartbeat $T_h = 1/1.35 = 0.741$

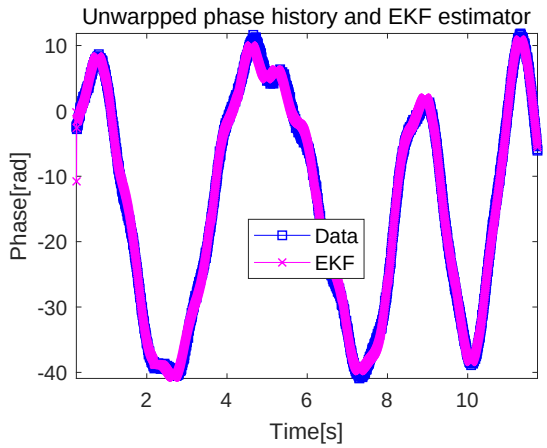

(a) Phase history tracking

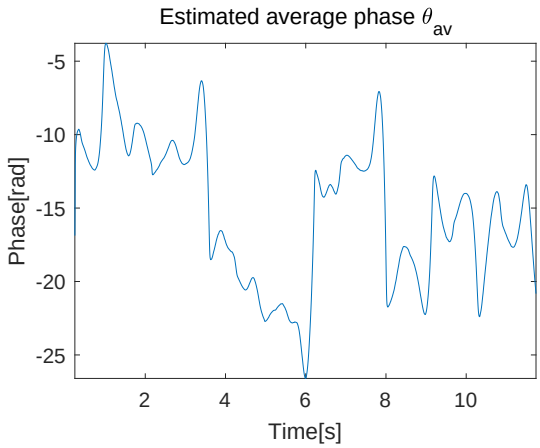

(b) Estimated average phase θ_{av}

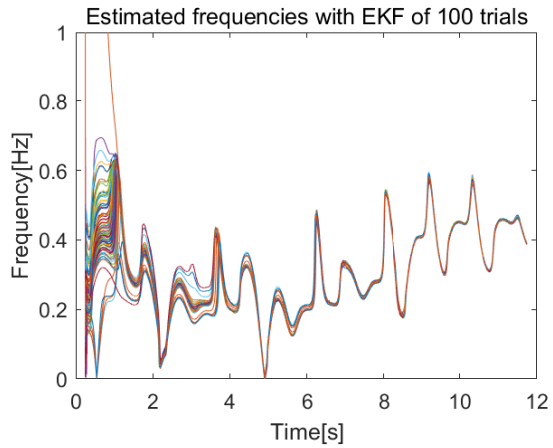

(c) Estimated frequencies of 100 trials

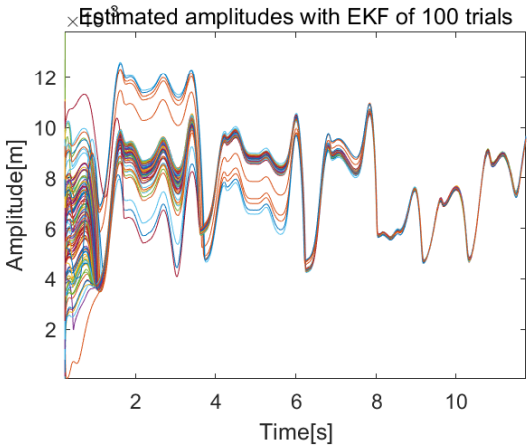

(d) Estimated amplitudes of 100 trials

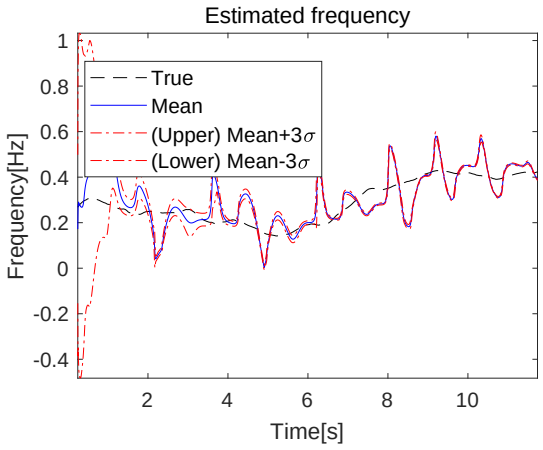

(e) Mean frequency and its variance

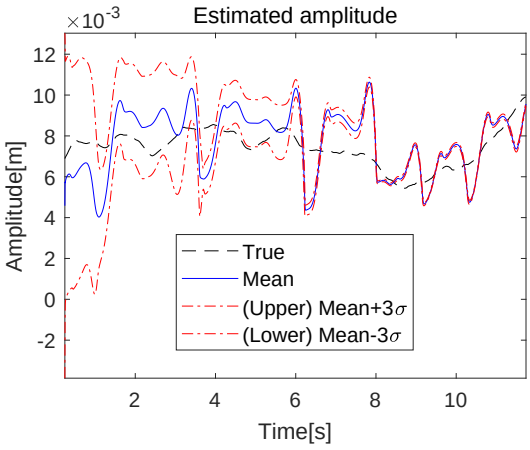

(f) Mean amplitude and its variance

Figure 4.24: EKF estimator for dynamic respiratory frequency and amplitude based on phase history of 100 trials (Dynamic f_r and α_r, $f_h = 1.35$ Hz and $\alpha_h = 0.5$ mm, $SNR_{pulse} = 10$ dB)

s. This is because that both of the state model and observation model of this EKF estimator does not include the existence of heartbeat activity which is regarded as noise

perturbation over time.

With the PF estimator for respiration based on phase history, the simulation result, with $SNR_{pulse} = 10$ dB and the annealing factor of $\alpha_w = 0.986$, is shown in Figure 4.25.

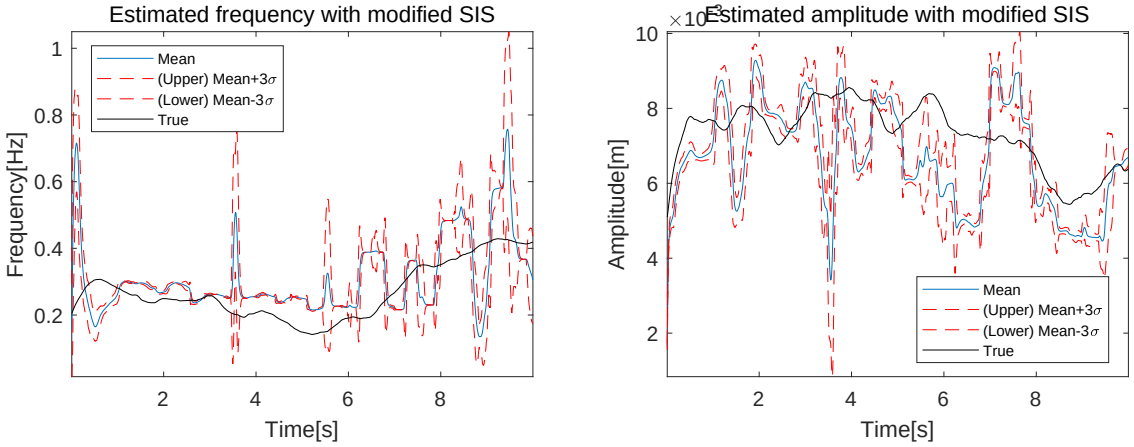

(a) Mean frequency and its variance

(b) Mean amplitude and its variance

Figure 4.25: PF estimator with modified SIS algorithm for dynamic respiratory frequency and amplitude based phase history of 100 trials (Dynamic f_r and α_r, $f_h = 1.35$ Hz and $\alpha_h = 0.5$ mm, $SNR_{pulse} = 10$ dB)

It can be observed from Figure 4.25 that, based on the phase history of the slow-time signal, the PF estimator suffers from the same problem with the EKF estimator that the estimated mean frequency and amplitude fluctuates around their true values according to the period of heartbeat $T_h = 0.741$ s. Besides, deviations of the estimated frequency and amplitude of the PF estimator from their true values are larger since the estimated average phase θ_{av} and the initial phase φ_r is incorrect in the initialization stage and cannot change to compensate the dynamic amplitude of wave.

4.3. Conclusion

In this chapter, the performance of two methods described in the last chapter, namely Extended Kalman filter and particle filter, has been evaluated in numerical simulations.

For Kalman filter, two models are considered based on the assumption of phase noise, non-Gaussian and Gaussian. One assumption is that with lower SNR SNR_{pulse} for each pulse, the phase noise is non-Gaussian. The real and imaginary part of the complex Gaussian noise are mutually independent, thus the noise of phase term does not follow a real-valued Gaussian distribution. Therefore, the observation based on the I/Q demodulation of the signal is considered and the noise for both real and imaginary part of the measured signal are Gaussian. Five unknown parameters, namely frequency ω, amplitude α, initial phase φ of the respiration activity and magnitude h and extra

phase ϕ_e caused by the distance and reflection coefficients of the measured target, are estimated simultaneously with this estimator. The simulation results show that the EKF estimator based on I/Q demodulation are not reliable and does converge on the true value with one data samples for each iteration. With increasing the number of the data samples for each iteration $k = 100$, the EKF estimator becomes stable and is able to track dynamic frequency and amplitude of respiration with $SNR_{pulse} = 5$ dB. Increasing the value of SNR_{pulse} does not always help stable the estimator. This is because the EKF estimator can converge around the sidelobes occurring in the ambiguity function with higher value of SNR_{pulse}. The estimator perform with lower value of SNR_{pulse} can perform better with the sidelobes buried below the noise level. The other assumption is that the value of SNR_{pulse} is considered to be above 8 dB and the noise for the unwrapped phase history is assumed to be Gaussian. With this assumption, the unwrapped phase history of the beat signal is the measured data and only 4 parameters are estimated, frequency ω, amplitude α, initial phase φ of the respiration activity and the average phase θ_{av} occurring in the unwrapped phase history influenced by the target distance, initial phase of respiration and reflection coefficient of the target. Simulation results show that the EKF estimator can track both constant and dynamic parameters with the number of the data samples for each iteration $k = 100$ and $SNR_{pulse} = 10$ dB. With the lower value of SNR_{pulse} to be 6 dB, the estimator fluctuates and the variance of the estimated parameters can be reduced by increasing the number of the data samples for each iteration k since the number of the data samples for each iteration contributes to the process gain of the measured data.

With the implementation of particle filter, sequential PF with modified SIS with an annealing factor $\alpha_w = 0.986$ is able to estimate the desired information on vital signs with dynamic frequency. The drawback of the weight degeneracy problem with the SIS algorithm is alleviated by adding the annealing factor α_w on the importance weights before its propagation.

With $SNR_{pulse} = 10$ dB, successful estimation for respiratory frequency and amplitude can be done with the existence of heartbeat activity by implementing EKF estimator based on phase history with $k + 1 = 101$. The EKF estimator based I/Q demodulation fails to estimate the desired parameters for respiration since the existence of sidelobes in the ambiguity function and heartbeat perturbation which cannot be regarded as noise. The PF estimator with modified SIS and initialization based on phase history fails to track dynamic amplitude since only two variables are considered in this estimator. The computational complexity and time increased dramatically with the increased number of variables which are used to correct the wrong the average phase θ_{av} and initial phase φ_r during the estimation.

Recommended further study is to estimate both vital signs simultaneously.

5

Experimental Estimation

In this chapter, the EKF estimator based on phase history with number of samples per iteration $k + 1 = 101$ is implemented on the experimental data for estimating the respiratory frequency and amplitude.

The radar is used in this experiment is shown in Figure 5.1.

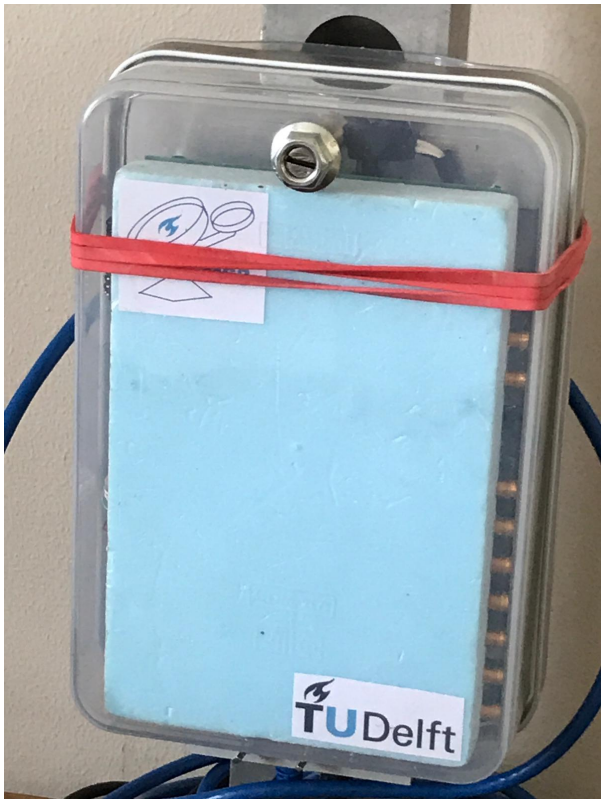

Figure 5.1: NXP Dolphin radar used

The parameters for in this experiment are presented in Table 5.1. The downsample factor of 128 is used to reduce size of the measured data and the PRF becomes 20 Hz for the final data.

Parameters	Values
Center Frequency	77 GHz
Set Bandwidth	1 GHz
PRI	65.1 μs
Coherent Bandwidth	920.4 MHz
PRI (Downsampled)	50 ms

Table 5.1: Radar parameters for experiment

The human under measure is sitting 2 m away from the radar as shown in Figure 5.2.

Figure 5.2: Measurement scenario

The measured range history and its power spectrum with one antenna is shown in Figure 5.3.

From Figure 5.3, it is shown that the shape of the chest movement due to respiration is approximately sinusoidal. The estimated frequency can be obtained by searching for the frequency peak in its power spectrum. And, the estimated frequency is 0.135 Hz.

The estimated frequency and amplitude for the respiration activity of the human is shown in Figure 5.4.

From Figure 5.4, it is observed that the EKF estimator with $k = 100$ based on phase history is able to track and estimate the respiratory frequency and amplitude sequentially as compared to the estimated result from Figure 5.3. The reason for the

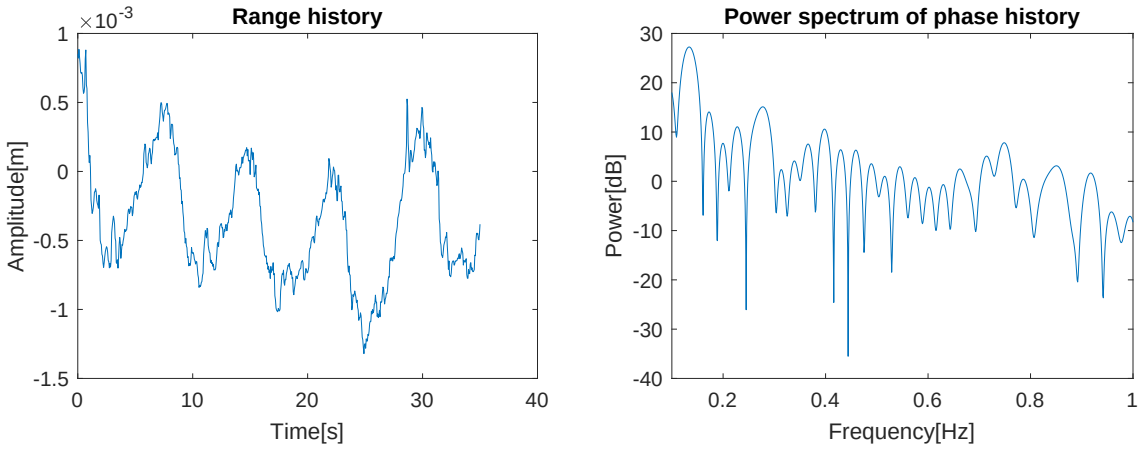

(a) Range history (b) Power spectrum

Figure 5.3: The measured range history and its power spectrum

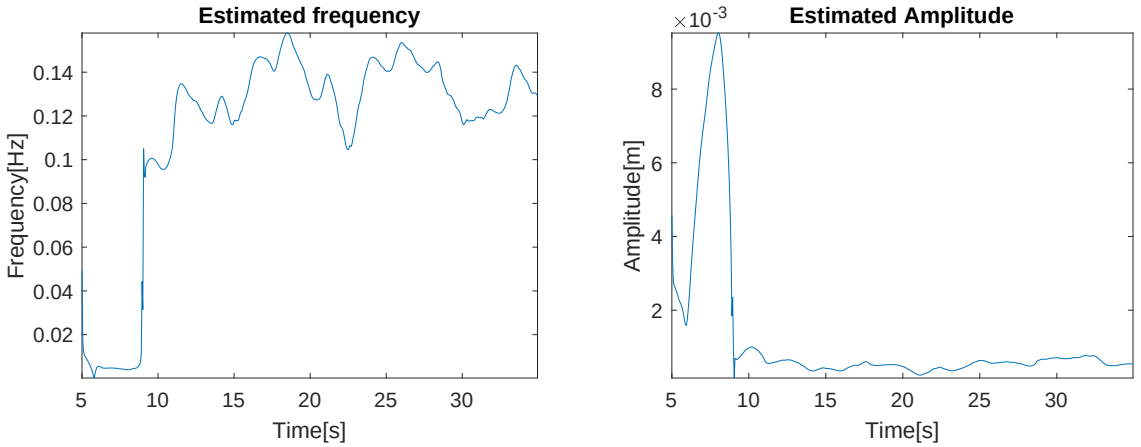

(a) Frequency (b) Amplitude

Figure 5.4: Estimated frequency and amplitude from real data

small estimated amplitude may be that the person under measure is relax and weak breathing activity leads.

6

Conclusion and Future Work

The topic of vital signs monitoring has drawn a great deal of concern nowadays. In the scenario of monitoring the health state of the driver and passengers in automotive, an LFMCW MIMO radar with center frequency $f_c = 77$ GHz is considered.

With the ability of LFMCW radar to measure the downrange distance and the ability of MIMO radar system to provide angular information, the space within the automotive can be meshed into 2D pixels. In this way, clutter from other pixels can be removed out from the desired pixels where targets are located. The vital signs of human within possible pixels are estimated and updated sequentially.

6.1. Results and Novelties

As the physiology of both vital signs presented briefly, it is known that the activities of both respiration and heartbeat can be measured by observing the movement of a human chest. Assuming that the RCS and the position of the desired target is constant during the measurement time, the information of vital signs is presented in the phase history $\phi_{ph}(n)$. These activities can be recovered from the phase history $\phi_{ph}(n)$ by implementing the phase unwrapping algorithm provided that coherence of the radar system is maintained.

The movement of both vital signs is modelled as sin, $|\sin|$ and $(\sin)^2$. The ambiguity function of the signal for each model is investigated. For all models, sidelobes level is $[-10, -5]$ dB below the mainlobe with CPI equal to $12s$.

Considering the movement of respiration is modelled as sin shape, NCF model is used for the estimation. Estimations of the frequency and amplitude of the respiration are simulated with two different methods, namely extended Kalman filter and particle

filter. With one observation sample for each iteration, the EKF estimator based on I/Q demodulation of the complex signal is unstable and not reliable. Increasing the number of the observation samples for each iteration to be $k+1 = 151$ thus increasing process gain, this estimator is able to estimate the frequency and amplitude of respiration activity with low SNR of each transmitted pulse, $SNR_{pulse} = 5$ dB and $SNR_{pulse} = 0$ dB. When it comes to the case of dynamic frequency and amplitude, the most of the estimator out of 100 trials can track the dynamic parameters as well as the mean of the 100 trials. The probability that the estimation lies around the true value of the frequency within 0.1 Hz increased as the time goes. Increasing the value of SNR_{pulse} can cause the estimator to be unstable or not reliable due to the existence of the sidelobes in the ambiguity function. Therefore, initial guess for this EKF estimator is important.

With the number of the observation samples for each iteration to be $k+1 = 101$, the EKF estimator performs well and stable to track both constant and dynamic frequency and amplitude of respiration based on the unwrapped phase history under the assumption that the value of SNR_{pulse} is larger than 6 dB and phase noise can be regarded as Gaussian. The number of unknown parameters is reduced from 5 to be 4 as compared to the EKF estimator based on I/Q demodulation of the complex signal. Since there is not sidelobes for sinusoidal movement, increasing the number of the observation samples for each iteration or the SNR for each transmitted pulse can give better performance for this estimator. However, certain mismatch occurs with the existence of longer observation window for each iteration which averages the measured frequencies.

Simulation result for PF with SIS algorithm shows the convergence of the estimated parameters, thus successful tracking of vital signs. However, This algorithm functions well only when the parameters are constant over time and is modified to track dynamic parameters with annealing factor of $\alpha_w = 0.985$ with the value of SNR_{pulse} larger than 6 dB. This is because that the importance weights propagate by multiplying with newly obtained importance weights and some values becomes extremely large while other becoming negligible as the estimators goes and the annealing factor can relieve the phenomenon. For this particle filter considered, certain initialization has been done in this simulation exercise, including estimating the initial phase φ of respiration and the average phase θ_{av} in the unwrapped phase history. Since the computational complexity and time increased dramatically for SIR algorithm and limitation of computational memory in the software Matlab, SIR is not tested in the thesis.

6.2. Recommendations for Future Research

Based on what has been learned in this exercise, some recommendations for future research are proposed as follows:

- Proper modelling for both respiration and heartbeat. Real movement of the two vital signs is not simply sinusoidal. With more accurate model, the estimation based on experimental data is considered to perform better.
- Exploring the relationship between respiration rate and heartbeat rate. This relationship can be used to further reduce the complexity of estimating both vital signs simultaneously and/or increase the reliability of estimation results.
- Check other possible models if sinusoidal model contained in the phase term of complex signal is considered. NCF gives good performance for a single real-valued sinusoidal model in [34] but it is not a perfect model for a sinusoidal wave contained in phase of complex signal.
- Particle filter with other effective algorithms. Since there are many unknown parameters to be estimated thus a great deal number of particles are processed for each iteration, effective algorithm help to reduce the computational complexity and time.

Bibliography

[1] J. Lin and C. Li, "Wireless non-contact detection of heartbeat and respiration using low-power microwave radar sensor," in *2007 Asia-Pacific Microwave Conference*. IEEE, 2007, pp. 1–4.

[2] J. C. Lin, "Applying telecommunication technology to health-care delivery," *IEEE Engineering in Medicine and Biology Magazine*, vol. 18, no. 4, pp. 28–31, July 1999.

[3] P. K. Capp, P. L. Pearl, and D. Lewin, "Pediatric sleep disorders," *Primary Care: Clinics in Office Practice*, vol. 32, no. 2, pp. 549–562, 2005.

[4] H. Forster, O. Ipsiroglu, R. Kerbl, and E. Paditz, "Sudden infant death and pediatric sleep disorders," 2003.

[5] N. Hafner, I. Mostafanezhad, V. M. Lubecke, O. Boric-Lubecke, and A. Host-Madsen, "Non-contact cardiopulmonary sensing with a baby monitor," in *2007 29th Annual International Conference of the IEEE Engineering in Medicine and Biology Society*. IEEE, 2007, pp. 2300–2302.

[6] J. C. Lin, "Noninvasive microwave measurement of respiration," *Proceedings of the IEEE*, vol. 63, no. 10, pp. 1530–1530, Oct 1975.

[7] H. Lee, B.-H. Kim, and J.-G. Yook, "Path loss compensation method for multiple target vital sign detection with 24-GHz FMCW radar," in *2018 IEEE Asia-Pacific Conference on Antennas and Propagation (APCAP)*. IEEE, 2018, pp. 100–101.

[8] T. Sakamoto, R. Imasaka, H. Taki, T. Sato, M. Yoshioka, K. Inoue, T. Fukuda, and H. Sakai, "Feature-based correlation and topological similarity for interbeat interval estimation using ultrawideband radar," *IEEE Transactions on Biomedical Engineering*, vol. 63, no. 4, pp. 747–757, 2015.

[9] M. Mercuri, P. J. Soh, G. Pandey, P. Karsmakers, G. A. Vandenbosch, P. Leroux, and D. Schreurs, "Analysis of an indoor biomedical radar-based system for health monitoring," *IEEE Transactions on Microwave Theory and Techniques*, vol. 61, no. 5, pp. 2061–2068, 2013.

[10] R. F. Martin, "Ultra-wideband (uwb) rules and design compliance issues," in *2003 IEEE Symposium on Electromagnetic Compatibility. Symposium Record (Cat. No. 03CH37446)*, vol. 1. IEEE, 2003, pp. 91–96.

[11] A. G. Yarovoy, J. Matuzas, B. Levitas, and L. P. Ligthart, "UWB radar for human being detection," in *European Radar Conference, 2005. EURAD 2005.*, Oct 2005, pp. 85–88.

[12] S. Jefremov and B. Levitas, "On application of a pulse method in detecting living objects," in *12th International Conference on Microwaves and Radar. MIKON-98. Conference Proceedings (IEEE Cat. No.98EX195)*, vol. 3, May 1998, pp. 765–768 vol.3.

[13] A. Aubert, L. Welkenhuysen, J. Montald, L. De Wolf, H. Geivers, J. Minten, H. Kesteloot, and H. Geest, "Laser method for recording displacement of the heart and chest wall," *Journal of biomedical engineering*, vol. 6, no. 2, pp. 134–140, 1984.

[14] C. Li, J. Lin, and Y. Xiao, "Robust overnight monitoring of human vital signs by a non-contact respiration and heartbeat detector," in *2006 International Conference of the IEEE Engineering in Medicine and Biology Society*. IEEE, 2006, pp. 2235–2238.

[15] P. Pahl, T. Kayser, M. Pauli, and T. Zwick, "Evaluation of a high accuracy range detection algorithm for FMCW/phase radar systems," in *The 7th European Radar Conference*, Sep. 2010, pp. 160–163.

[16] K. Konno and J. Mead, "Measurement of the separate volume changes of rib cage and abdomen during breathing," *Journal of applied physiology*, vol. 22, no. 3, pp. 407–422, 1967.

[17] T. Sakamoto, P. J. Aubry, S. Okumura, H. Taki, T. Sato, and A. G. Yarovoy, "Noncontact measurement of the instantaneous heart rate in a multi-person scenario using X-band array radar and adaptive array processing," *IEEE Journal on Emerging and Selected Topics in Circuits and Systems*, vol. 8, no. 2, pp. 280–293, June 2018.

[18] J. Aho, J. Salmi, and V. Koivunen, "Adaptive processing and realistic signal propagation modeling for multiantenna vital sign radar," in *2013 IEEE Radar Conference (RadarCon13)*, April 2013, pp. 1–6.

[19] S. Wang, A. Pohl, T. Jaeschke, M. Czaplik, M. Köny, S. Leonhardt, and N. Pohl, "A novel ultra-wideband 80 GHz FMCW radar system for contactless monitoring of

vital signs," in *2015 37th Annual International Conference of the IEEE Engineering in Medicine and Biology Society (EMBC)*, Aug 2015, pp. 4978–4981.

[20] S. Ayhan, S. Diebold, S. Scherr, A. Tessmann, O. Ambacher, I. Kallfass, and T. Zwick, "A 96 GHz radar system for respiration and heart rate measurements," in *2012 IEEE/MTT-S International Microwave Symposium Digest*, June 2012, pp. 1–3.

[21] F. Adib, H. Mao, Z. Kabelac, D. Katabi, and R. C. Miller, "Smart homes that monitor breathing and heart rate," in *Proceedings of the 33rd annual ACM conference on human factors in computing systems*. ACM, 2015, pp. 837–846.

[22] I. V. Mikhelson, S. Bakhtiari, T. W. Elmer, and A. V. Sahakian, "Remote sensing of patterns of cardiac activity on an ambulatory subject using millimeter-wave interferometry and statistical methods," *Medical & biological engineering & computing*, vol. 51, no. 1-2, pp. 135–142, 2013.

[23] M. Mercuri, Y.-H. Liu, I. Lorato, T. Torfs, F. Wieringa, A. Bourdoux, and C. Van Hoof, "A direct phase-tracking doppler radar using wavelet independent component analysis for non-contact respiratory and heart rate monitoring," *IEEE transactions on biomedical circuits and systems*, vol. 12, no. 3, pp. 632–643, 2018.

[24] C. Li and J. Lin, "Random body movement cancellation in doppler radar vital sign detection," *IEEE Transactions on Microwave Theory and Techniques*, vol. 56, no. 12, pp. 3143–3152, 2008.

[25] B.-K. Park, O. Boric-Lubecke, and V. M. Lubecke, "Arctangent demodulation with dc offset compensation in quadrature doppler radar receiver systems," *IEEE transactions on Microwave theory and techniques*, vol. 55, no. 5, pp. 1073–1079, 2007.

[26] V. Singh, S. Bhattacharyya, and P. Jain, "Through the wall human signature detection using principle component analysis (pca)," in *2018 IEEE International Symposium on Antennas and Propagation & USNC/URSI National Radio Science Meeting*. IEEE, 2018, pp. 1975–1976.

[27] M. Xu, A. Goldfain, J. DelloStritto, and S. Iyengar, "An adaptive kalman filter technique for context-aware heart rate monitoring," in *2012 Annual International Conference of the IEEE Engineering in Medicine and Biology Society*. IEEE, 2012, pp. 6522–6525.

[28] Y. Yu, W. Yin, L. Li, and L. Zhang, "Vital sign integrated tracking by predictive knn and kalman filter with UWB radars," in *2018 10th International Conference on Wireless Communications and Signal Processing (WCSP)*. IEEE, 2018, pp. 1–6.

[29] S. Groot, R. Harmanny, H. Driessen, and A. Yarovoy, "Human motion classification using a particle filter approach: multiple model particle filtering applied to the micro-Doppler spectrum," *International Journal of Microwave and Wireless Technologies*, vol. 5, no. 3, pp. 391–399, 2013.

[30] W. G. Carrara, R. S. Goodman, and R. M. Majewski, "Spotlight synthetic aperture radar signal processing algorithms," 1995.

[31] J. E. Hall, *Guyton and Hall textbook of medical physiology*. Elsevier Health Sciences, 2006.

[32] F. Weishaupt, I. Walterscheid, O. Biallawons, and J. Klare, "Vital sign localization and measurement using an LFMCW MIMO radar," in *2018 19th International Radar Symposium (IRS)*. IEEE, 2018, pp. 1–8.

[33] G. Wang, J. Muñoz-Ferreras, C. Gu, C. Li, and R. Gómez-García, "Linear-frequency-modulated continuous-wave radar for vital-sign monitoring," in *2014 IEEE Topical Conference on Wireless Sensors and Sensor Networks (WiSNet)*, Jan 2014, pp. 37–39.

[34] W. Ng, C. Ji, W. Ma, and H. C. So, "A study on particle filters for single-tone frequency tracking," *IEEE Transactions on Aerospace and Electronic Systems*, vol. 45, no. 3, pp. 1111–1125, 2009.

[35] S. M. Kay, *Fundamentals of Statistical Signal Processing: Estimation Theory*. Prentice Hall PTR, 1993.

[36] A. Doucet, N. De Freitas, and N. Gordon, *Sequential Monte Carlo Methods in Practice*. Springer Publishing, New York, 2001.

[37] Z. Chen *et al.*, "Bayesian filtering: From kalman filters to particle filters, and beyond," *Statistics*, vol. 182, no. 1, pp. 1–69, 2003.

[38] N. J. Gordon, D. J. Salmond, and A. F. Smith, "Novel approach to nonlinear/non-Gaussian Bayesian state estimation," in *IEEE proceedings F (radar and signal processing)*, vol. 140, no. 2. IET, 1993, pp. 107–113.